DEPARTMENT OF AEROSPACE ENGINEERING

TECHNION Israel Institute of Technology

Lattice Boltzmann method simulations of the laminar flow in a two-dimensional double cavity configuration

Research Project
Author: Itamar Blumenfeld
Advisor: Dr. Hadar Ben Gida
Faculty of Aerospace Engineering
Technion Israel Institute of Technology, Haifa 3200003, Israel
March 23, 2025

Abstract

The flow through two opposing open cavities, referred to as a double cavity configuration, is a well-documented phenomenon observed in various contexts, including sudden expansions and contractions in pipe flows, as well as the exit of confined jets. In this configuration, the dynamic interaction between the two shear layers emerging from each wall of the inlet channel is significantly influenced by both the cavity and the channel dimensions. This study investigates the characteristics of a two-dimensional laminar and incompressible flow within the double cavity configuration, utilizing an in-house Lattice Boltzmann Method (LBM) code. The LBM is an evolving and well-documented methodology rooted in kinetic theory, with numerous versions available for implementation. The in-house LBM code employs either a Bhatnagar-Gross-Krook (BGK) or a two-relaxation-time (TRT) model as the collision operator, the bounce-back (BB) method as an obstacle boundary condition, the Zou-He scheme for domain boundary conditions, and the D2Q9 discrete velocity set. The code is first validated with two prominent and extensively documented cases. The first case involves the canonical flow over a two-dimensional circular cylinder, and the second concerns the flow around a two-dimensional square cylinder positioned in a channel. In both validation scenarios, we examined the pressure coefficient distribution on the bluff bodies (cylinder or square), the resultant lift and drag coefficients, and the Strouhal number associated with the vortex shedding in the wake behind the bodies. A good agreement was obtained between the numerical LBM solver results and the reference results utilized for comparison. A double cavity configuration was later studied based on the successful validation of the in-house LBM solver. The double cavity configuration investigated herein has a cavity length-to-hight ratio (L/H) of 2 and a non-dimensional channel width (D/L) of 0.2 and was studied for a range of cavity length-based Reynolds numbers (Re_L) from 3600 to 10000. The results showed good agreement with the available data in the literature and were analyzed to assess the impact of the Reynolds number on the laminar flow regimes in the double cavity configuration.

Nomenclature

Δt	Time step size
Δx	Lattice spacing
Ω	Collision operator
ρ	Fluid density
τ	Relaxation parameter
$\vec{\xi}$	Particle mesoscopic velocity vector
$\vec{c}_i$	Discrete velocity vector
$\vec{x}$	Location vector
C_D	Drag coefficient
C_L	Lift coefficient
C_p	Pressure coefficient
c_s	Speed of sound
f	Particle distribution function
f^{eq}	Particle equilibrium distribution function
Re	Reynolds number
St	Strouhal number
w_i	Weight parameters
BB	Bounce-back
BE	Boltzmann transport equation
BGK	Bhatnagar, Gross, and Krook
CBC	Characteristic boundary conditions
CFD	Computational fluid dynamics
FFT	Fast Fourier transform
LBE	Lattice Boltzmann equation
LBGK	Lattice BGK equation
LBM	Lattice Boltzmann method
LE	Leading edge
NSE	Navier-Stokes equations
NS	Navier-Stokes
PSD	Power spectral density
RHS	Right-hand side
TE	Trailing edge
TRT	Two-Relaxation-Time

1 Introduction

The flow within open cavities involves complex dynamics, which, depending on the flow regime, can be highly sensitive to various factors such as compressibility and turbulence. One common flow mechanism occurs when the shear layer impacts the downstream rear wall of the cavity, generating upstream-propagating acoustic waves that excite the shear layer and lead to self-sustained oscillations. These oscillations are directly dependent on the flow regime, determined by the Reynolds number and the cavity geometry (length-to-depth ratio), and are recognized as the noise source in many applications. For compressible flow conditions, where the acoustic wavelength is comparable to the shear layer impingement length (cavity length), accounting for the acoustic speed is essential to determine the time delay between pressure fluctuations on the impinged rear wall surface and at the shear-layer separation point. For incompressible open cavity flows, where the acoustic wavelength is much greater than the impingement length, alternative mechanisms, which are purely hydrodynamic, are assumed to have a more significant role. This has been confirmed by experimental investigations conducted on water flow (Burroughs and Stinebring (1994)) and air (Lusseyran et al. (2008); Basley et al. (2011)), which also validate the hypothesis that the same phenomenon is expected to manifest in both water and air flows at low Mach numbers. This study will focus only on the laminar flow mechanisms that occur in incompressible conditions and will validate their characteristics.

When two open cavities are placed in a channel facing each other, a double cavity configuration is established, which may lead to dynamic interactions between the shear layers originating from each wall of the inlet channel as illustrated in Fig. 1. Such flows are relevant to a variety of industrial and biomechanical applications, including sudden expansions and contractions in pipe flows (Drikakis (1997)), the structure of scramjets for enhanced combustion efficiency (Du et al. (2023)), the exit dynamics of confined jets (Maurel et al. (1996); Righolt et al. (2015)), and the impact of optical properties on photonic crystals (Wang et al. (2020)). A comprehensive understanding of the flow dynamics in double cavity configurations is essential for applications in both engineering and natural systems.

The study by Tuerke (2017) examines the double cavity configuration using both experimental and numerical methods across various flow regimes and cavity geometries. The flow entering the channel determines the characteristics of the velocity profile at the leading edge of the cavities. The flow regime, as discussed in Tuerke et al. (2017), was confined to scenarios where the inflow profile exhibited laminar characteristics, such as the laminar Poiseuille flow. This constraint was implemented to eliminate potential fluctuation excitations associated with turbulent flows. The geometric characteristics of the double cavity configuration were determined by the channel height D, the cavity depth H, and the cavity length L (see Fig. 1). From time series data derived from velocity signals obtained through two-dimensional numerical simulations, Tuerke et al. (2017) found that the velocity signal from a single probe was sufficient to capture the main characteristics of the global flow behavior. Furthermore, Tuerke et al. (2017) assert that, based on results obtained through two-dimensional numerical simulations, the cavity length-based Reynolds number $Re_L = U_\infty L/\nu$, where U_∞ is the maximum inflow velocity and ν is the kinematic viscosity, has a significant effect on the flow regimes observed for a given D/L ratio. Such flow regimes range from steady to periodic,

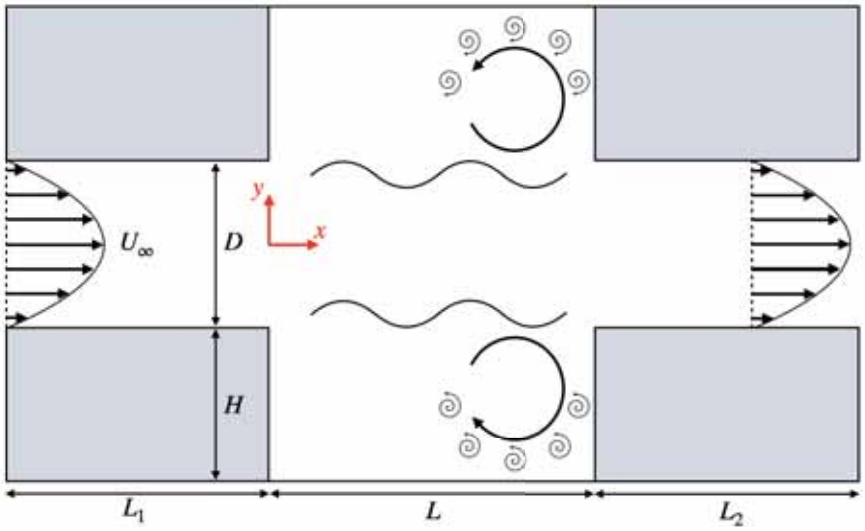

Figure 1: A schematic representation of the flow within the double cavity configuration. D denotes the channel height, H is the cavity depth, L is the cavity length, and L_1 and L_2 refer to the lengths of the inlet and outlet channels, respectively.

intermediate, and ultimately chaotic as Re_L increases. The authors used the cavity length-based Strouhal number $St_L = fL/U_\infty$ to analyze the quasi-steady results in the phase space, where f is the signal frequency.

Maurel et al. (1996) studied a planar jet entering a large cavity, a geometry that is analogous to the double cavity configuration. The experimental setup incorporated an inlet channel with a height-to-cavity depth ratio of $D/H = 1/12$, with the cavity length L as the primary variable. The authors identified three distinct flow regimes: a stable regime exhibiting no oscillations, a self-sustained oscillation regime, and a regime that is characterized by turbulent free jet behavior. Within the self-sustained oscillation regime, the flow was predominantly two-dimensional, and the authors further classified it into two categories: a sinuous mode featuring large-scale wavelengths and a varicose mode exhibiting shorter wavelengths. The scenario characterized by a constant ratio of L/H and varying values of D has not been investigated by Maurel et al. (1996). Nevertheless, an increase in the ratio of D/H leads to a significant extension of the two shear layers, thereby preventing their confluence along the length of the cavity, subsequently giving rise to a double cavity flow. For sufficiently large values of D, it is anticipated that the flow behavior characteristic of a single cavity is expected to reappear.

The laminar flow within the system discussed above can be simulated utilizing various computational and numerical methods. Recently, Tuerke (2017) employed a numerical method that is based on the incompressible and isothermal non-dimensional Navier-Stokes equations (NSE), as outlined by Gadoin et al. (2001), Podvin et al. (2006), and Rizi et al. (2015). The current study aims to investigate the laminar and incompressible flow in a similar double cavity geometry, employing an alternative computational approach - the Lattice Boltzmann Method (LBM). LBM is a computational fluid dynamics (CFD) technique that models fluid behavior through a mesoscopic approach based on the Boltzmann equation rather than directly solving the macroscopic Navier-Stokes equations. LBM has various strengths and weaknesses, depending on the problem and the flow regime to be solved. According to Krüger et al. (2017) and Viggen (2014), LBM is highly suitable for simulating

fluid dynamic problems involving aeroacoustic phenomena. However, it is known to be less effective for solving compressible flows in the high supersonic regime. Selecting the LBM for resolving the laminar flow within a double cavity configuration is highly attractive, as the method can effectively capture the self-sustained flow oscillations present within the configuration.

In this study, an in-house LBM code was developed, implemented in MATLAB, and verified against generic flow cases. The first validation case involves the two-dimensional laminar flow over a circular cylinder subjected to a uniform flow stream, which was compared to the findings presented by Lienhard et al. (1966), Zdravkovich (1990), Zdravkovich (1997) and Norberg (2001). The second validation case involves the two-dimensional laminar flow over a square cylinder placed in the middle of a channel subjected to fully developed channel flow, which was compared to results by Breuer et al. (2000) and Zhou et al. (2005). For both validation cases, the in-house LBM solver showed good agreement with the available data from the literature in terms of the integral aerodynamic coefficients, mean pressure distribution, and vortex shedding frequencies, thus confirming the numerical framework developed herein.

With the in-house LBM solver validated, the code was then utilized to solve the case of a double rectangular cavity configuration, where the flow field results were compared to recently published results by Tuerke (2017). Four distinct simulations were conducted utilizing a fixed double-cavity geometry, with the distinguishing factor being the cavity length-based Reynolds number Re_L. The flow field in the double cavity configuration was simulated for Reynolds numbers (Re_L) of 3600, 5100, 7000, and 10000, with the objective of capturing four distinct flow regimes that are characteristic of this geometry under laminar flow: steady, periodic, intermediate, and chaotic. Initially, a visual analysis of the resulting flow fields was conducted to classify the observed flow phenomena and structures in each regime and compare these findings with established results. A more detailed examination of the flow field solution was performed for the simulation corresponding to the periodic flow regime ($Re_L = 5100$). Eight probes were positioned within the cavity region (similar to those used by Tuerke (2017)) and utilized to record the horizontal velocity throughout the duration of the simulation. The signals were analyzed spectrally to better understand the characteristics and nature of the observed phenomena within the cavity region for this flow regime, including the shear layer oscillations and the frequency of the large re-circulation region in the cavities. A comparative analysis was then conducted by examining the horizontal velocity signals recorded at a specific probe and their spectral analysis across all four tested flow regimes. This comparison reveals that the Reynolds number has a significant influence on the properties and characteristics of the flow structures developing within the flow field. The computed results were compared with published data in the literature, aiming to validate the classification of the flow regimes identified by the in-house LBM solver. Aside from a slight discrepancy in the Reynolds numbers classifying the different flow regimes, the LBM solver successfully captured all predicted flow regimes, confirming its ability to resolve such complex flow dynamics.

2 The computational method - LBM

2.1 Boltzmann Transport Equation

The computational flow method utilized in this research is the Lattice Boltzmann Method (LBM), which is based on the Boltzmann transport equation (BTE). This method is a type of kinetic theory application that is employed in various contexts. This equation is applied at the mesoscopic length scale, which lies between the microscopic and macroscopic scales being much smaller than the macroscopic scale but significantly larger than the microscopic one. Therefore, the fundamental variable in kinetic theory, and in particular in the BE, is the particle distribution function $f(\vec{x}, \vec{\xi}, t)$. This variable represents the density of particles with the mesoscopic velocity $\vec{\xi}$ at location $\vec{x}$ and time t. The BTE describes the evolution of the distribution function in time and, thus, can be derived from the total time derivative of f:

$$\frac{\mathrm{d}f}{\mathrm{d}x} = \frac{\partial f}{\partial t} + \xi_i \frac{\partial f}{\partial x_i} + \frac{F_i}{\rho}\frac{\partial f}{\partial \xi_i} = \Omega(f). \tag{1}$$

The term F_i/ρ represents the specific body force, and the right-hand side (RHS) term is a source term that describes the local redistribution of f due to collisions. Therefore, $\Omega(f)$ is called the collision operator. While many formulations exist for the collision operator, one of the most common and simple forms is the Bhatnagar, Gross, and Krook (BGK) collision operator. Note that the collision operator formulation of the BGK model must consider the conservation of mass, momentum, and energy by ensuring that the moments of $\Omega(f)$ will be zero. The BGK collision operator is derived as follows:

$$\Omega(f) = -\frac{1}{\tau}(f - f^{eq}), \tag{2}$$

where two fundamental variables are used in this formulation. The first is the particle equilibrium distribution function (f^{eq}). This variable describes the state of the fluid in equilibrium; in other words, when a fluid is undisturbed for a sufficient time, it can be assumed that the distribution function f will reach an equilibrium distribution f^{eq}. The second is the relaxation parameter (τ), which describes the relaxation time towards the equilibrium state. The macroscopic properties of the fluid (e.g., density ρ and macroscopic velocity $\vec{u}$) can be computed from the BTE by taking the moments of the equation; i.e., by multiplying it with $\vec{\xi}$ and integrating over the velocity space, as shown in Eq. (3) where the index α denote the direction of the macroscopic and mesoscopic velocities ($\vec{u}$ and $\vec{\xi}$, respectively).

$$\rho = \int f \mathrm{d}^3\xi \quad ; \quad \rho u_\alpha = \int \xi_\alpha f \mathrm{d}^3\xi. \tag{3}$$

Several methods and approaches exist to solve the BTE. The main objective is calculating the distribution function f, which allows for computing the fluid's macroscopic properties. This goal is crucial, as with many other CFD methods, thus motivating the discretization and numerical solution of the BTE.

2.2 Lattice Boltzmann Equation

The LBM solves the lattice Boltzmann equation (LBE), which is derived by discretizing the BTE in space, velocity, and time. In this context, the discrete-velocity distribution function $f_i(\vec{x}, t)$ serves as the fundamental variable in the LBE, where i denotes the index of the discrete velocity. Essentially, f_i characterizes the density of a particle having a discrete velocity $\vec{c}_i = (c_{i,x}, c_{i,y}, c_{i,z})$ at position $\vec{x}$ and time t. The points where f_i is defined are arranged in a spatial square lattice with lattice spacing Δx and are defined at specific times every time step Δt. The prevailing choice in LBM involves *lattice units*, which refer to a straightforward artificial unit system where $\Delta x = 1$ and $\Delta t = 1$. Various discrete velocity sets within a square lattice are typically represented as DdQq, where d denotes the number of spatial dimensions the velocity set encompasses, and q denotes the set's quantity of velocities. In this study, the D2Q9 velocity set is used for the 2D flow simulations, as shown in Fig. 2.

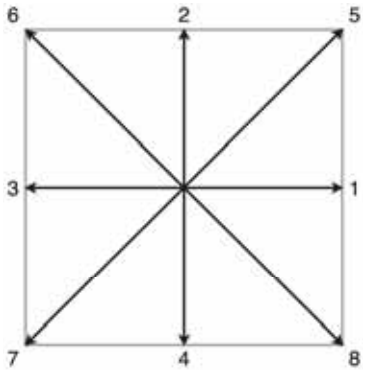

Figure 2: D2Q9 velocity set

At each node of the 2D square lattice domain, the eight discrete velocities are directed at each neighboring node, while the zero index velocity describes a stationary particle (at the center). Every velocity set for LBM is defined by two sets of quantities: the velocities $\vec{c}_i$ and the corresponding weights w_i. The velocity vector $\vec{c}_i$ defines the discrete set of possible directions and speeds at which particles can move in the lattice space; this velocity vector is a discretized form of the mesoscopic velocity $\vec{\xi}$. The weights parameters w_i ensure the macroscopic properties (e.g., mass and momentum) are correctly recovered when averaging the mesoscopic dynamics. In essence, they reflect the contribution of each discrete velocity to the overall distribution function. These $\vec{c}_i$ and w_i are critical because they determine the connectivity between lattice nodes and the method's accuracy. The values of these quantities for the D2Q9 velocity set are presented in table 1.

i	0	1	2	3	4	5	6	7	8
w_i	4/9	1/9	1/9	1/9	1/9	1/36	1/36	1/36	1/36
$c_{i,x}$	0	+1	0	−1	0	+1	−1	−1	+1
$c_{i,y}$	0	0	+1	0	−1	+1	+1	−1	−1

Table 1: D2Q9 velocity set in explicit form; i.e., the weight parameter w_i and the discrete velocity $\vec{c}_i$ for each of the nine possible directions

In section 2.1, it was shown that the macroscopic fluid properties can be extracted from the solution of the BTE by taking the moments of f_i (see Eq. (3)). For the discretized form of the equations, LBE, the macroscopic fluid properties are computed as follows:

$$\rho \;=\; \sum_i f_i(\vec{x},t) \quad ; \quad \rho\vec{u}(\vec{x},t) \;=\; \sum_i \vec{c}_i f_i(\vec{x},t). \tag{4}$$

Generally, by calculating the discrete distribution function and assigning the correct values for velocity and weight for the corresponding velocity set, the macroscopic fluid properties can be computed; therefore, discretization must be done to the BTE to obtain the $f_i(\vec{x},t)$. Discretizing the Boltzmann equation in velocity space, physical space, and time leads to the *lattice Boltzmann equation*, written below:

$$f_i(\vec{x}+\vec{c}_i\Delta t, t+\Delta t) = f_i(\vec{x},t) + \Omega_i(\vec{x},t). \tag{5}$$

As with BTE, the LBE affects the particle distribution at the next time step and location with the collision operator Ω_i. The simplest form of this operator (BGK) can be used for Navier-Stokes (NS) simulations.

$$\Omega(f_i) \;=\; -\frac{f_i - f_i^{eq}}{\tau}\Delta t. \tag{6}$$

Same as the collision operator in the BE, the collision operator in the LBE relaxes the populations towards an equilibrium f_i^{eq} at a rate determined by the relaxation time τ, and its discrete form is given by:

$$f_i^{eq} \;=\; w_i\rho\left(1 + \frac{\vec{u}\cdot\vec{c}_i}{c_s^2} + \frac{(\vec{u}\cdot\vec{c}_i)^2}{2c_s^4} - \frac{\vec{u}\cdot\vec{u}}{2c_s^2}\right). \tag{7}$$

The constant c_s is associated with each chosen velocity set in the basic isothermal LBE. In this framework, c_s governs the relation $p = c_s^2\rho$, linking the pressure p to the density ρ. As a result, it can be demonstrated that c_s corresponds to the speed of sound in the isothermal model. For the velocity set used here (D2Q9), this constant is given by $c_s^2 = (1/3)\Delta x^2/\Delta t^2$. Same as the discrete distribution function f_i, the moments of the discrete equilibrium distribution function f_i^{eq} yields the macroscopic fluid properties i.e. $\sum_i f_i^{eq} = \sum_i f_i = \rho$ and $\sum_i \vec{c}_i f_i^{eq} = \sum_i \vec{c}_i f_i = \rho\vec{u}$. There is a big difference between the BTE and the Navier-Stokes equations (NSE), but they are strongly correlated under various assumptions. This relationship can be established using the Chapman-Enskog analysis, demonstrating that the LBE leads to macroscopic behavior consistent with the NSE, where the kinematic shear viscosity is expressed in terms of the relaxation time τ as:

$$\nu \;=\; c_s^2\left(\tau - \frac{\Delta t}{2}\right). \tag{8}$$

Although some LBM algorithms incorporate a multi-relaxation time (MRT) parameter τ in simulations, in this study, a constant relaxation time or two-relaxation time (TRT) will be employed in the simulations. Using a constant relaxation time results in a uniform kinematic viscosity throughout all flow domains. By using a two-relaxation-time (TRT) model, one can integrate the algorithmic

simplicity of the BGK operator with enhanced accuracy and stability properties involving more complex models. Furthermore, the TRT model requires only two relaxation rates: the first relaxation rate is associated with the shear viscosity (ω^+) and relaxes the moments related to even-order polynomials, while the second serves as a free parameter (ω^-) and relaxes the moments related to odd-order polynomials. The TRT incorporates the capability to control the accuracy and stability of the simulation through the use of the Λ parameter, defined as follows:

$$\Lambda = \left(\frac{1}{\omega^+ \Delta t} - \frac{1}{2}\right)\left(\frac{1}{\omega^- \Delta t} - \frac{1}{2}\right). \tag{9}$$

The parameter Λ characterizes the truncation error and the stability properties of the TRT model, and it can be chosen empirically. As described in Krüger et al. (2017) for $\Lambda = 1/12$, the parameter effectively cancels the third-order spatial error, yielding optimal outcomes for pure advection problems. In the case of $\Lambda = 1/6$, the parameter cancels the fourth-order spatial error, thus delivering the most precise results for the pure diffusion equation. Furthermore, for $\Lambda = 3/16$, this parameter results in the boundary wall location implemented via bounce-back method for Poiseuille flow, positioned precisely in the center between horizontal walls and fluid nodes. Lastly, for $\Lambda = 1/4$, this parameter ensures the most stable simulations. The TRT model solves the Navier-Stokes equation with kinematic shear viscosity

$$\nu = c_s^2 \left(\frac{1}{\omega^+ \Delta t} - \frac{1}{2}\right). \tag{10}$$

In this manner, the parameter ω^- is regarded as a free parameter while Λ is selected empirically, and ω^+ is computed using equation Eq. (10). By obtaining the two relaxation parameters ω^+ and ω^-, the distribution function for the next time step can be computed, as will be explained later.

2.3 The time step

In the previous section, we discussed the formulation of the discretized BTE, known as LBE, and how its discrete mesoscopic properties are connected to the macroscopic flow properties. Additionally, to describe the flow evolution in time, the time-step scheme must be derived in the discrete time-space. In the LBE (see Eq. (5)), the discrete distribution function f_i is updated in the next time step depending on the collision operator Ω_i. By choosing the BGK collision operator (as seen in Eq. (6)), the LBE (Eq. (5)) can be re-written as follows:

$$f_i(\vec{x} + \vec{c}_i \Delta t, t + \Delta t) \;=\; f_i(\vec{x}, t) - \frac{\Delta t}{\tau}\left(f_i(\vec{x}, t) - f_i^{eq}(\vec{x}, t)\right). \tag{11}$$

The equation above is referred to as the lattice BGK equation (LBGK) equation, and it represents the full discretization of the BTE utilizing the BGK collision operator. As mentioned, this equation described the evolution of f_i in time and space. For practical purposes, the equation can be decomposed into two steps. In the first step, the values of f_i undergo an update in accordance with a specific collision operator. At each discrete point within the spatial domain, the value of f_i is subject to modification yet remains untransformed to any neighboring point. This process is termed the *collision step*, with the resultant discrete distribution function being denoted as $f_i^\star$, as shown in Eq. (12). In the second step, the updated values of $f_i^\star$ are propagated to the neighboring points according to the discrete velocity direction. Specifically, within the D2Q9 velocity set, the

updated value may be transmitted in any of the nine possible directions within the 2D domain. This process is commonly known as the *streaming step*. Consequently, in this second step, the value of $f_i^\star$ can be assigned to the value of f_i at the corresponding neighboring point in the next time step, as depicted in Eq. (13). After both steps, the distribution function's value is concurrently updated in both temporal and spatial domains.

$$f_i^\star(\vec{x},t) \;=\; f_i(\vec{x},t) - \frac{\Delta t}{\tau}\left(f_i(\vec{x},t) - f_i^{eq}(\vec{x},t)\right) \tag{12}$$

$$f_i(\vec{x}+\vec{c}_i\Delta t, t+\Delta t) \;=\; f_i^\star(\vec{x},t) \tag{13}$$

If the TRT collision model is employed, the LBE will have an alternate form. To implement the TRT model, one needs to decompose the populations (f_i) and equilibrium populations (f_i^{eq}) into their symmetric and antisymmetric parts, accordingly:

$$\begin{aligned} f_i^{+} &= \frac{f_i + f_{\bar{i}}}{2}, \quad f_i^{-} = \frac{f_i - f_{\bar{i}}}{2} \\ f_i^{\mathrm{eq}+} &= \frac{f_i^{\mathrm{eq}} + f_{\bar{i}}^{\mathrm{eq}}}{2}, \quad f_i^{\mathrm{eq}-} = \frac{f_i^{\mathrm{eq}} - f_{\bar{i}}^{\mathrm{eq}}}{2}, \end{aligned} \tag{14}$$

where $f_{\bar{i}}$ and $f_{\bar{i}}^{\mathrm{eq}}$ represent the populations and the equilibrium populations corresponding to the opposite discrete velocities of f_i and f_i^{eq}, respectively. By achieving the symmetric and antisymmetric parts of the populations and the equilibrium populations, the two steps of the LBE with the TRT collision operator can be implemented similarly to the BGK model:

$$\begin{aligned} f_i^\star(\vec{x},t) \;&=\; f_i(\vec{x},t) - \omega^+\Delta t\left(f_i^+ - f_i^{\mathrm{eq}+}\right) - \omega^-\Delta t\left(f_i^- - f_i^{\mathrm{eq}-}\right), \\ f_i(\vec{x}+\vec{c}_i\Delta t, t+\Delta t) &= f_i^\star(\vec{x},t). \end{aligned} \tag{15}$$

Overall, the two steps described represent the decomposition of the LBE in BGK and TRT collision models, where these are illustrated in Fig. 3. This explicit formulation facilitates the advancement of the flow solution in both spatial and temporal domains, ultimately leading to the derivation of a simple algorithm for the LBM.

2.4 Solid Boundaries conditions

Until now, we have explored how, through the use of LBE, we can assess flow properties at each spatial location at any given time step without introducing physical disturbances in the flow domain, such as bodies and objects. Accordingly, it is imperative to employ some boundary conditions to accurately account for an obstacle placed within the flow field. On the solid boundary, two fundamental conditions are requisite for viscous flow: a *no-slip* condition, mandating that the tangential velocity is zero at the boundary, and a *impermeable* condition, mandating that the normal velocity is zero at the boundary. The bounce-back (BB) method is one of the most straightforward and longstanding boundary conditions utilized in LBM. The fundamental principle of the BB method dictates that, during the streaming step, when a particle encounters a rigid wall, it undergoes reflection, returning to its original position. The *no-slip* and *impermeable* boundary conditions may

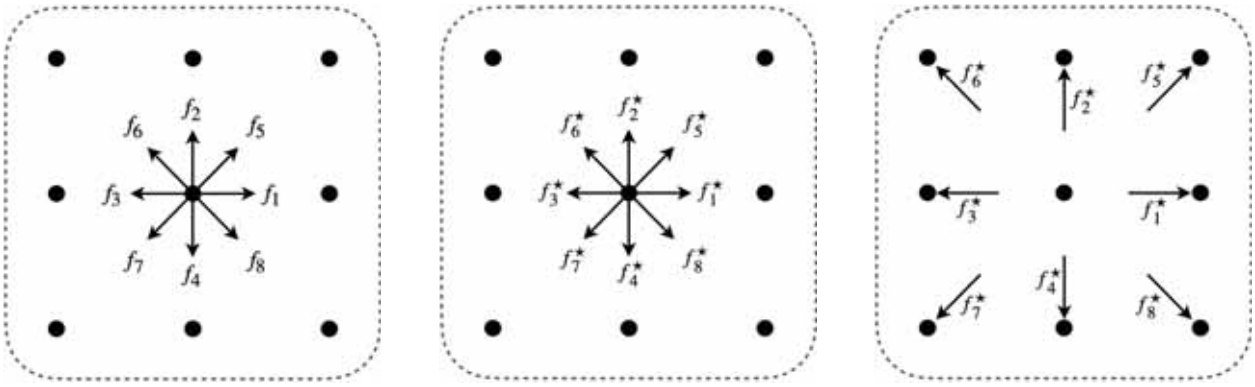

(a) (b) (c)

Figure 3: The time step process focuses on a single point. (a) Pre-collision: At this stage, the point has nine values of the particle distribution function. (b) Post-collision: The values of the particle distribution function at the same point are updated according to the collision operator. (c) Streaming: The updated values of the particle distribution function are transferred to the corresponding neighboring points.

not seem intuitive at first, but they can be understood by considering fluid particles as portions of fluid matter. When particles bounce back after hitting a wall (as illustrated in Fig. 4), this implies there is no fluid flux across the boundary, meaning the wall is impermeable (*impermeable* condition is applied). Additionally, since particles are reflected back rather than forward, it indicates there is no relative motion between the fluid and the wall, meaning no slip occurs (*no-slip* condition is applied). This bounce-back method mimics the Dirichlet boundary condition for zero velocity at the wall.

Figure 4: Illustration of the bounce-back boundary condition of a fluid particle on an arbitrary solid wall.

2.5 In-house LBM solver framework

In the present study, an in-house LBM solver framework has been developed to investigate flow phenomena across various obstacles and domains. This section introduces the LBM code, its underlying algorithms, and how they are implemented in the solver framework. A flowchart is provided at the end of this section in Fig. 5 to better visualize the LBM solver framework. Generally, the LBM solver framework is divided into three stages, each explained separately below.

2.5.1 Stage 1: Pre-processing

In the initial phase, we define all requisite inputs for the simulations. This encompasses the characteristic length scale (D), freestream velocity (U_∞), length scale-based Reynolds number (Re_D), and the total number of simulation iterations (N). It is essential to recognize that all units are defined within the "lattice world". Specifically, the length units represent the distance between adjacent nodes (Δx), while the time unit corresponds to the iteration number. The selection of these specific units can be rationalized by the flow regime present in the examined simulation. Given that the simulation is designed to deal only with **incompressible** and **laminar** flow, the corresponding normalized NSE solely depends on the non-dimensional parameter, the Reynolds number. As previously noted, the NSE is correlated with the LBE through the Chapman-Enskog analysis. Consequently, in LBM simulations conducted within these flow regimes, the choice of units (whether lattice or physical) is inconsequential; the outcomes depend solely on the Reynolds number.

Next, in this stage, the domain mesh is generated based on the obstacle under examination. A detailed description of the domain generation for each case is provided in the results chapter. The fundamental concept of constructing the mesh is that it comprises a two-dimensional binary array containing only the values 0 or 1. The value 0 represents nodes within the domain where the flow is defined, whereas the value 1 denotes nodes within the domain where the solid body is defined. With this structure, one can know exactly where the BB boundary condition should be applied in the domain to implement *impermeable* and *no-slip* boundary conditions.

Moreover, during this stage, we define and compute all requisite flow parameters, specifically the speed of sound (c_s), kinematic viscosity (ν), and time relaxation (τ). As previously indicated, the speed of sound in LBM simulation is given by $c_s = 1/\sqrt{3}$, under the condition that Δt and Δx are both equal to 1 ($c_s^2 = (1/3)\Delta x^2/\Delta t^2$). The kinematic viscosity is computed by the Reynolds number definition, where $Re = U_\infty D/\nu$, and the time relaxation τ or ω^+ is computed in accordance with Eq. (8) or Eq. (10), respectively, depending on whether the BGK or TRT collision model is employed.

Finally, for this stage, we delineate all parameters associated with the LBM parameters, including the velocity set parameters (D2Q9: $d = 2$, $q = 9$), the velocity vector c_i, the weight vector w_i, the lattice indices (0, 1, 2, ...), and supplementary parameters that provide added utility, such as, arrays that describe the lattice indices the describe the velocity with a component in the left, right, upward, or downward direction.

2.5.2 Stage 2: Initialization

During the second stage, we establish the initial values for the properties under examination. These properties include the velocity profile ($\vec{u}$), fluid density (ρ), and particle distribution function (f) fields. First, the initial value of the density field has been chosen to be $\rho(\vec{x}, t = 0) = 1$, since it is the typical choice for this initial macroscopic field (Krüger et al. (2017)). The initial value of the velocity field depends upon the specific type of simulation conducted. In this study, two distinct flow types within the two-dimensional domain were analyzed for validation. The first analysis involves a uniform flow field surrounding an obstacle, while the second involves the two-dimensional Poiseuille flow (fully developed flow) in a channel with an obstacle placed within. The velocity profile field

was initialized differently for each flow type, as specified below.

1. **Uniform flow field:** The velocity profile field, $\vec{u} = (u, v)$, was set merely with a streamwise velocity component u that equals to the freestream velocity U_∞; i.e., $u(\vec{x}, t = 0) = U_\infty$, and $v(\vec{x}, t = 0) = 0$.
2. **Poiseuille flow field:** The velocity profile field was established based on the analytical solution of a fully developed laminar flow within a channel with a pressure gradient, also known as the Poiseuille flow. The analytical solution yields a parabolic velocity profile in the channel, which, with the coordinate system situated at the middle of the channel, is expressed as follows:

$$u(y) = U_\infty \left(1 - \frac{4y^2}{D^2}\right) \quad ; \quad v(y) \; = \; 0, \tag{16}$$

   where u represents the streamwise component, v denotes the normal component of the initial velocity field, and D signifies the width of the channel.

Finally, the initial particle distribution function field shall be established in accordance with the computed equilibrium distribution function (f^{eq}) that corresponds to the initial density and velocity profile field. It is important to note that based on a specified density and velocity field, the equilibrium distribution function can be computed by Eq. (7).

2.5.3 Stage 3: The time step

The main stage of the algorithm is the time step loop. During this phase, the values of the particle distribution function (f) are updated across all two-dimensional domains and subsequently compute the macroscopic properties (ρ and $\vec{u}$) at a given time step. This stage is the main core of the LBM solver framework. For clarity, the time step stage will be divided into several distinct sub-steps, as detailed below.

1. **Current macroscopic properties:** First, the current macroscopic properties, specifically ρ and $\vec{u}$, are determined based on the particle distribution function from the previous time step (or the initial f if referring to the first iteration). The current macroscopic properties shall be calculated by evaluating the first and second moments of f, as previously elucidated and demonstrated in Eq. (4).

2. **Inflow/Outflow BC:** Next, the inflow and outflow boundary conditions in the domain are being enforced. These boundary conditions maintain the requisite inlet flow throughout all time steps and ensure that the outlet boundary does not introduce upstream-propagating reflections of the fluid into the computational domain. The implementation of such boundary conditions differs between the two distinct types of flow regimes explored in this study, namely uniform flow and Poiseuille flow fields. Additionally, two specialized boundary conditions may be incorporated as necessary, contingent upon the specific problem being addressed.
   - **Uniform flow field:** For this type of flow field, the boundary condition was applied for both the inlet and outlet of the computational domain. Initially, a uniform velocity value is computed at the inlet, corresponding to the initial velocity profile field. Specifically, in each iteration, a uniform streamwise velocity U_∞ is enforced at the inlet, with zero normal

velocity component. The density field is computed based on the Dirichlet boundary condition, based on the Zuo/He scheme (see Zou and He (1996)). Following this scheme, the density field at the inlet ρ_{in} is computed as follows:

$$\rho_{in} = \frac{f_0 + f_2 + f_4 + 2(f_3 + f_6 + f_7)}{1 - u_{in}}, \tag{17}$$

where $f_0,\ f_2,\ f_4$ represent the vertical particle distribution functions, whereas $f_3,\ f_6,\ f_7$ denote the particle distribution functions that extend outward from the domain (see Fig. 3a), and u_{in} is the streamwise velocity at the inlet. The last property to define at the inlet is the particle distribution function. According to Zou and He (1996), the ingoing (right) particle distribution function f at the inlet (f_1, f_5, and f_8) is equivalent to the ingoing (right) equilibrium distribution function f^{eq}; i.e., $f_1 = f_1^{eq},\ f_5 = f_5^{eq},\ f_8 = f_8^{eq},$. This condition is implemented following a subsequent step, where the f^{eq} is computed. The outlet boundary condition is computed based on the Neumann boundary condition, stating that the variation in the left-oriented (inward-facing) particle distribution function remains constant about the streamwise axis.

- **Poiseuille flow field:** In this type of flow field, the analytical solution of the velocity profile from Poiseuille flow in a channel is applied at the inlet. To achieve the above, the macroscopic density and velocity boundary conditions are applied at the inlet and outlet boundaries. These macroscopic conditions are implemented following Zou and He (1996). The inlet velocity profile (u_{in}) is established based on the analytical solution expressed in Eq. (16), enforcing a parabolic streamwise velocity profile that represents a laminar flow within a channel with a pressure gradient. The normal inlet velocity is zero ($v_{in} = 0$). The density field at the inlet (ρ_{in}) is applied similarly to the uniform flow field BC, as described in Eq. (17). The density at the outlet will be set to one, thus preventing the flow from returning upstream into the computational domain ($\rho_{out} = 1$). The streamwise velocity at the outlet will be set similarly to Eq. (17), as follows:

$$u_{out} = 1 - \frac{f_0 + f_2 + f_4 + 2(f_1 + f_5 + f_8)}{\rho_{out}}. \tag{18}$$

It is observed that the left-facing particle distribution function ($f_3,\ f_6,\ f_7$) has been replaced with a right-facing distribution function ($f_1,\ f_5,\ f_8$), as the boundary condition is now applied at the outlet. Additionally, the normal velocity at the outlet will be set to zero ($v_{out} = 0$).

Determining the mesoscopic boundary conditions at both the inlet and outlet is essential. At the inlet, the mesoscopic boundary condition is exclusively applied to the inward-facing particle distribution function, which, in this instance, corresponds to the right-oriented

particle distribution functions ($f_1,\ f_5,\ f_8$):

$$\begin{aligned} f_1 &= f_3 + \frac{2}{3}\rho_{in}u(y), \\ f_5 &= f_7 - \frac{1}{2}(f_2 - f_4) + \frac{1}{6}\rho_{in}u(y), \\ f_8 &= f_6 + \frac{1}{2}(f_2 - f_4) + \frac{1}{6}\rho_{in}u(y). \end{aligned} \tag{19}$$

Similarly, the mesoscopic boundary condition at the outlet is exclusively applied to the inward-facing particle distribution function, which, in this instance, is oriented to the left (denoted as $f_3,\ f_6,\ f_7$):

$$\begin{aligned} f_3 &= f_1 - \frac{2}{3}\rho_{out}u(y), \\ f_6 &= f_8 + \frac{1}{2}(f_4 - f_2) - \frac{1}{6}\rho_{out}u(y), \\ f_7 &= f_5 + \frac{1}{2}(f_2 - f_4) - \frac{1}{6}\rho_{out}u(y). \end{aligned} \tag{20}$$

- **Non-reflective BC:** Both the inlet and outlet boundary conditions previously discussed behave similarly to most boundary conditions in the LBM as they specify the velocity or density of the flow field at the inlet and outlet. Such boundary conditions are far from ideal for flows containing sound waves, as they will reflect sound waves back into the fluid. Consequently, any sound waves produced within the computational domain will not exit the system and can potentially pollute the simulation results. In geometries generating sound waves, such as cavities, it is essential to establish appropriate boundary conditions to mitigate these back-reflecting acoustic waves effectively. The non-reflective boundary condition established in the in-house LBM solve framework is the characteristic boundary conditions (CBC), as detailed in Krüger et al. (2017). This BC is based on the Euler conservation equations in both vector and matrix forms, which can be expressed for x-boundary (boundary for constant x) as follows:

$$\frac{\partial \boldsymbol{m}}{\partial t} \ = \ -\boldsymbol{P}_x^{-1}\mathcal{L}_x' - \gamma \boldsymbol{Y}\frac{\partial \boldsymbol{m}}{\partial y}, \tag{21}$$

where the fluid variable vector is $\boldsymbol{m} = [\rho,\ u_x,\ u_y]^T$. The $\boldsymbol{P}_x$ matrix (or $\boldsymbol{P}_y$) is an invertible matrix that can perform a diagonalization to the matrix $\boldsymbol{X}$ (or $\boldsymbol{Y}$) as $\boldsymbol{X} = \boldsymbol{P}_x^{-1}\boldsymbol{\Lambda}_x\boldsymbol{P}_x$ and it is defined accordingly:

$$\boldsymbol{P}_x = \begin{bmatrix} c_\mathrm{s}^2 & -c_\mathrm{s}\rho & 0 \\ 0 & 0 & 1 \\ c_\mathrm{s}^2 & c_\mathrm{s}\rho & 0 \end{bmatrix}, \quad \boldsymbol{P}_x^{-1} = \begin{bmatrix} \frac{1}{2c_\mathrm{s}^2} & 0 & \frac{1}{2c_\mathrm{s}^2} \\ -\frac{1}{2\rho c_\mathrm{s}} & 0 & \frac{1}{2\rho c_\mathrm{s}} \\ 0 & 1 & 0 \end{bmatrix}. \tag{22}$$

As this system of equations is hyperbolic, the matrices $\boldsymbol{X}$ and $\boldsymbol{Y}$ are diagonalizable and they are defined as follows:

$$\boldsymbol{X} = \begin{bmatrix} u_x & \rho & 0 \\ c_s^2/\rho & u_x & 0 \\ 0 & 0 & u_x \end{bmatrix}, \quad \boldsymbol{Y} = \begin{bmatrix} u_y & 0 & \rho \\ 0 & u_y & 0 \\ c_s^2/\rho & 0 & u_y \end{bmatrix}. \tag{23}$$

The $\mathcal{L}'_x$ is a characteristic vector, defined explicitly as:

$$\begin{aligned} \mathcal{L}_{x,1} &= (u_x - c_s)\left[c_s^2 \partial_x \rho - c_s \rho \partial_x u_x\right] \\ \mathcal{L}_{x,2} &= (u_x)\left[\partial_x u_y\right] \\ \mathcal{L}_{x,3} &= (u_x + c_s)\left[c_s^2 \partial_x \rho + c_s \rho \partial_x u_x\right]. \end{aligned} \tag{24}$$

for outgoing characteristics and zero ($\mathcal{L}_{x',i} = 0$) for ingoing characteristics. Finally, the scalar parameter γ is determined through empirical selection. According to Heubes et al. (2014), the optimal choice is $\gamma = 3/4$.

- **Buffer zone:** As a non-reflective boundary condition, the CBC is an effective method for minimizing the amplitude of reflective waves. However, it is important to note that the CBC does not entirely eliminate these waves. In geometries that are particularly sensitive to the generation of sound waves, such as cavities, weaker reflections from the boundaries may still be detected. To ensure no waves are reflected back from the boundaries, a buffer zone is applied at both the inlet and outlet boundaries. The buffer zone is a specialized region with high viscosity added to the computational domain near the boundaries. Its primary purpose is to minimize artificial reflections of waves, disturbances, or flow structures that may occur at the domain boundaries. In this in-house LBM solver, the buffer zone is adjusted gradually according to the cosine decay function $d(x)$ as follows:

$$d(x) \;=\; \frac{1}{2}\left(1 + \cos\left(\frac{\pi x}{l}\right)\right) \tag{25}$$

where l represents the buffer zone length, and x denotes the position within the buffer zone. The function is multiplied by an amplification factor, which governs the viscosity enhancement at the inlet and outlet boundaries compared to the characteristic viscosity in the domain. This approach incorporates two buffer zones into all the boundary conditions, serving as an additional tool to minimize the artificial reflection of waves.

3. **Equilibrium distribution function:** At this sub-step, the equilibrium particle distribution function f^{eq} is computed according to Eq. (7). Note that the density and velocity fields calculated from f^{eq} are employed in Eq. (7) after applying the boundary conditions, except for the case of the uniform flow regime, where the mesoscopic boundary conditions are determined only after the calculation of the f^{eq}, as they are dependent upon the updated value of f^{eq}.

4. **Collision - BGK/TRT:** At this sub-step, the fundamental component of each LBM algorithm will be established. The value of the particle distribution function after the collision and before

streaming (denoted as $f^{\star}$) is computed using the Bhatnagar-Gross-Krook (BGK) model or the Two-Relaxation-Time (TRT) model with the empirical selection of $\Lambda = 3/16$, as described in Eq. (12) and Eq. (15).

5. **Bounce-Back boundary condition:** At this sub-step, the surface boundary condition of the obstacle within the domain is implemented. As previously mentioned, the selected approach for addressing bodies and obstacles in this algorithm is the BB boundary condition. In this method, when the mesoscopic particle encounters the body's surface, it changes its direction to precisely the opposite of one of the nine possible velocity directions. Practically, the mesh is divided into two sections: fluid nodes (designated as 0) and body nodes (designated as 1). For each body node, the particle distribution function direction is modified to reflect the corresponding opposite direction. This operation must occur post-collision step and before the streaming step.

6. **Streaming:** In the final sub-step, the propagation of the particle to its corresponding neighboring node takes place. Each of the nine updated particle distribution function values (after considering the collision and BB boundary conditions for the relevant nodes) is transferred to the appropriate nodes. It is noteworthy that the shifting process is executed in a circular manner for the uniform flow field having no walls at the top and bottom boundaries; i.e., the particle distribution function that is oriented upwards at the upper boundary is transferred to the lower boundary and vice versa. This methodology simulates a flow domain with an obstacle possessing an infinite blockage ratio (the ratio of the domain width to the obstacle width) to prevent fluid reflections from the upper and lower boundaries, akin to walls.

2.5.4 Algorithm flowchart

A schematic flow chart of the solver algorithm is depicted in Fig. 5 to accompany the comprehensive description of the in-house LBM framework.

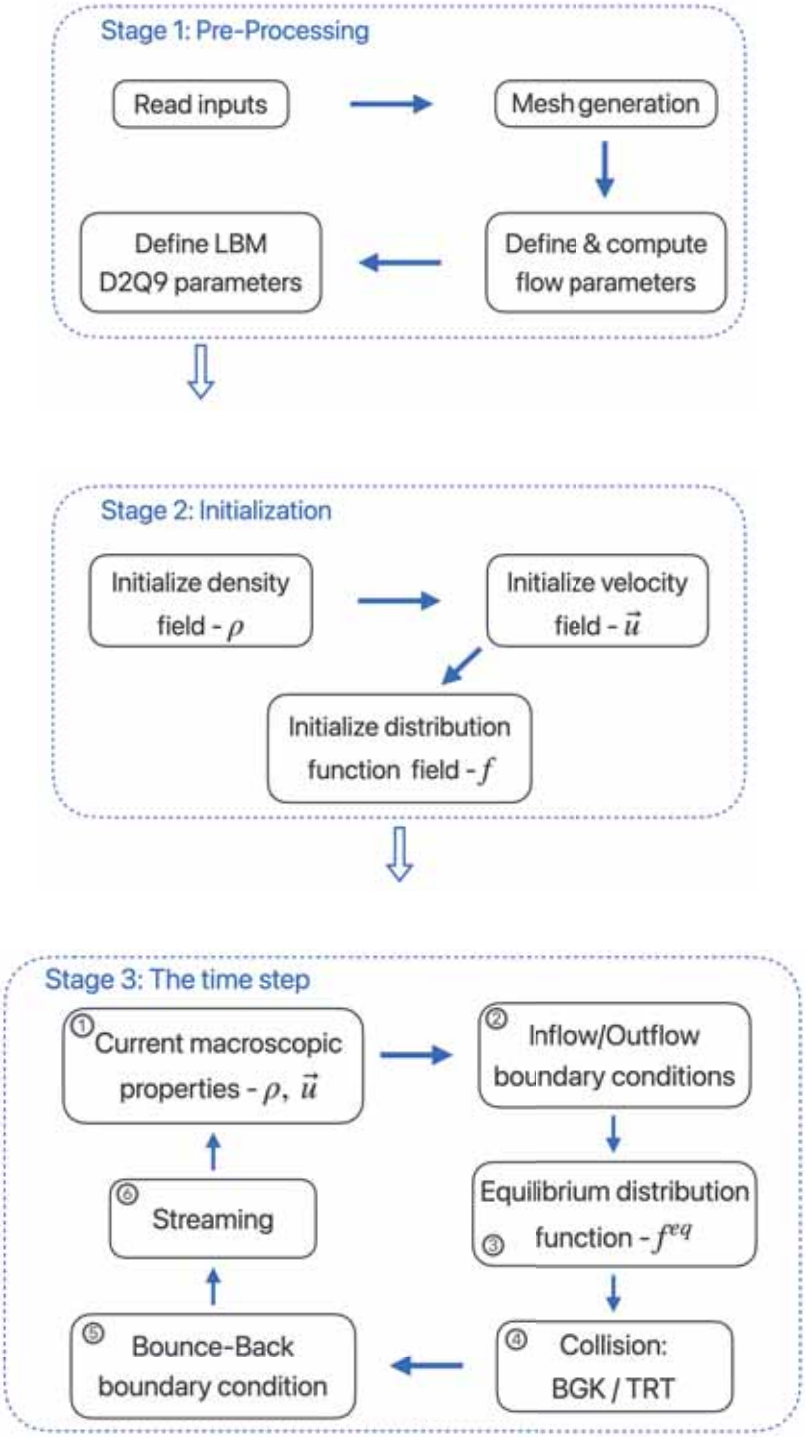

Figure 5: Flowchart of the in-house LBM solver algorithm

3 Results

This section presents the validation of the in-house LBM code for canonical and well-documented geometries. Consequently, the results for the double cavity configuration are presented and compared with existing results from the literature. For simplicity, the resulting flow properties presented in this section will be given in non-dimensional lattice units; i.e., the units addressed in this context will be the computational units, specifically iterations (as a temporal unit) and node distance (as a spatial unit). This methodology is appropriate given that the flow regime investigated herein is assumed to be laminar and incompressible, for which the non-dimensional incompressible NSE solely depends on the Reynolds number; thus, the Reynolds number is the only parameter that influences the flow characteristics. Notably, the primary equation in LBM is the LBE rather than the NSE. However, as previously mentioned, these equations are correlated via the Chapman-Enskog analysis.

3.1 Verification

3.1.1 2D laminar flow over a circular cylinder

The validation case presented here has been selected to provide a preliminary verification of the LBM scheme of the in-house code and to understand the methodology for obtaining the desired flow properties. These objectives will be accomplished by solving one of the most fundamental, widely investigated cases in fluid mechanics, specifically the two-dimensional laminar flow over a circular cylinder.

The computational domain is defined such that the cylinder, with a diameter of D, is positioned at a distance of 5 diameters from both the inlet, the upper and lower boundaries of the domain, and at a distance of 20 diameters from the outlet boundary, as illustrated in Fig. 6. The domain size was selected to adequately capture the shed vortices in the wake region and minimize reflections from the outlet boundary.

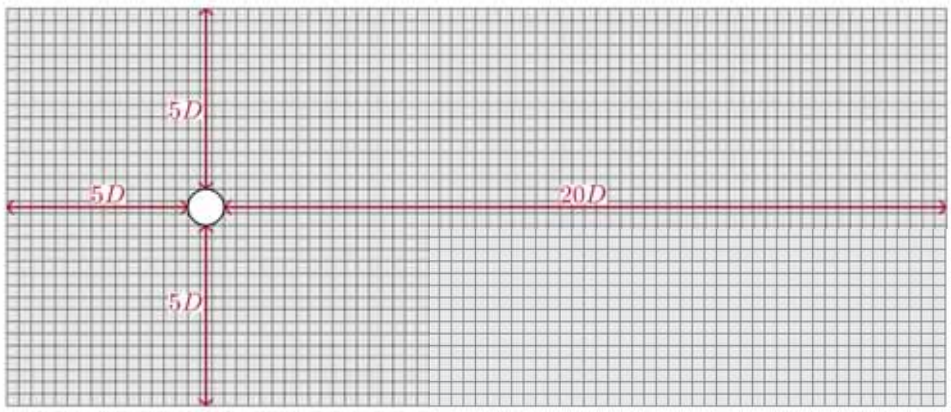

Figure 6: Computational domain of the two-dimensional circular cylinder case.

The LBM simulations were performed using the BGK collision model with a uniform horizontal

flow field, with a velocity of $U_\infty = 0.1$ [nodes/iteration]. This specific type of flow field was employed in the initial and boundary conditions, as detailed in section 2.5. The resolution was defined based on the cylinder diameter, set to $D = 30$ [nodes]. Consequently, the entire domain mesh was defined according to this resolution, as illustrated in Fig. 6. The freestream velocity and mesh resolution were chosen to achieve an optimal balance between runtime and result accuracy. The Reynolds number is defined based on the cylinder diameter, where $Re_D = 100$, from which the kinematic viscosity and the relaxation time of the simulation are computed according to $Re_D = U_\infty D/\nu$ and Eq. (8).

One of the fundamental flow characteristics the LBM solver has to capture at the simulated flow conditions is the vortex shedding behind the cylinder. In the real world, vortex shedding behind a cylinder occurs due to small disturbances in the flow field, which gradually cause oscillations in the separation points along the cylinder's surface, leading to vortex shedding. No apparent disturbances are observed in the case studied herein. Thus, the vortex-shedding phenomenon may originate from very small numerical errors that accumulate asymmetrically, ultimately acting as disturbances within the domain that generate vortex shedding. To study the vortex shedding behind the cylinder, the normalized velocity magnitude ($\frac{|\vec{u}|}{U_\infty}$) and the normalized vorticity magnitude ($\frac{|\vec{\omega}|}{U_\infty/D}$) fields are plotted, as shown in Fig. 7.

In the case studied herein, qualitatively, the vortex-shedding phenomenon seems to be successfully captured, as evidenced by the instantaneous flow field shown in Fig. 7, during which the flow is in a quasi-steady state. The vortices start to shed right from the separation region on the cylinder surface. Over time, the separation points (the upper and lower regions) on the cylinder surface move in opposite directions relative to each other, resulting in one vortex being shed from each separation region during each cycle. Generally, the shed vortices maintain a relatively constant size and distance from one another, which instills confidence in the ability of the LBM solver to simulate the phenomenon.

For a more quantitative validation, the time-averaged pressure coefficient distribution around the cylinder was computed from the LBM results and compared to existing literature from Zdravkovich (1997). The pressure coefficient was computed at any specified node within the mesh at a given moment by deriving the pressure field from the density field, as outlined in section 2.2 ($p = c_s^2\rho$), with the following definition:

$$C_p = \frac{p - p_\infty}{\frac{1}{2}\rho_\infty U_\infty} \tag{26}$$

where p represents the pressure at the designated node, and p_∞ and ρ_∞ denote the reference pressure and density, respectively. These parameters typically correspond to values recorded at significant distances from the area of interest, while U_∞ signifies the magnitude of the freestream velocity. In Fig. 8, the polar coordinate system surrounding the cylinder is presented to elucidate the position of each point on the cylinder's surface in relation to the leading edge (LE) and the trailing edge (TE) of the cylinder. With the appropriate definition of the relevant coordinate system, the results of the time-averaged pressure coefficient distribution $\bar{C}_p(\theta)$ can be adequately compared, as presented in Fig. 9.

Generally, a good agreement is shown between the LBM results and the experimental data

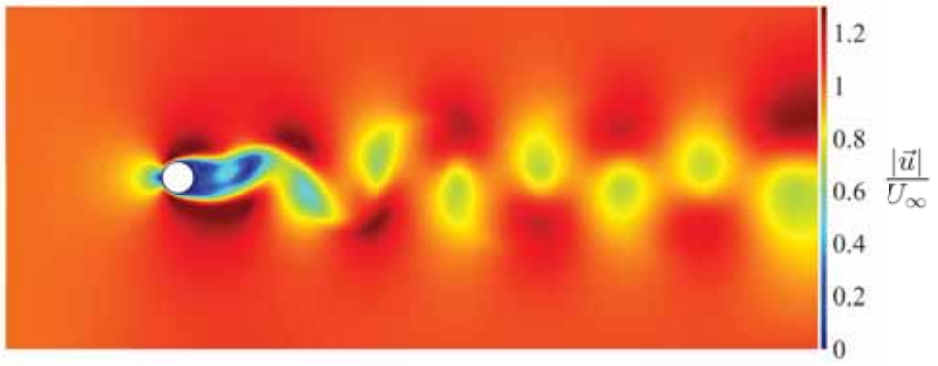

(a)

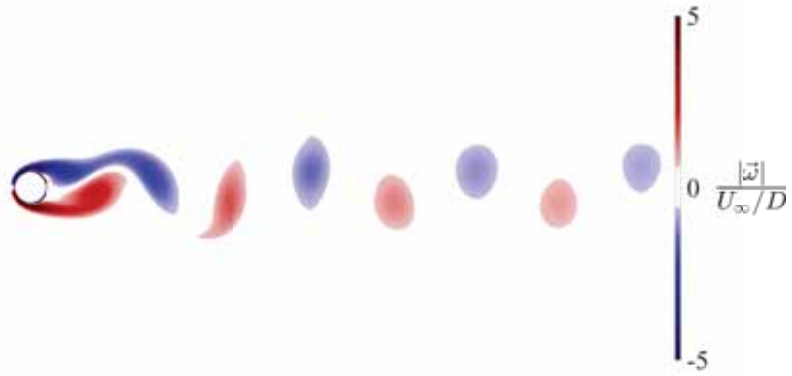

(b)

Figure 7: Instantaneous flow field around a circular cylinder (iteration 200,000) for $Re_D = 100$. (a) Contour plot of the normalized velocity magnitude. (b) Contour plot of the normalized vorticity magnitude.

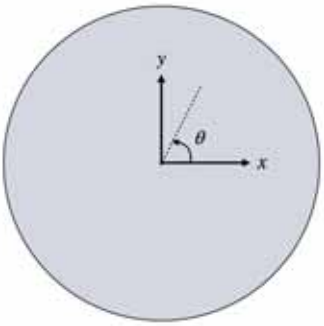

Figure 8: Polar coordinate system of the 2D circular cylinder. The polar angle θ defines the location on the surface of the cylinder, measured counterclockwise from the positive x-axis.

published by Zdravkovich (1997). In the right (downstream) half-cylinder ($-90° < \theta < 90°$), the mean pressure coefficient closely aligns between the two sets of results. In the left (upstream) half-cylinder ($-180° < \theta < -90°$ and $90° < \theta < 180°$), a significant increase in the mean pressure

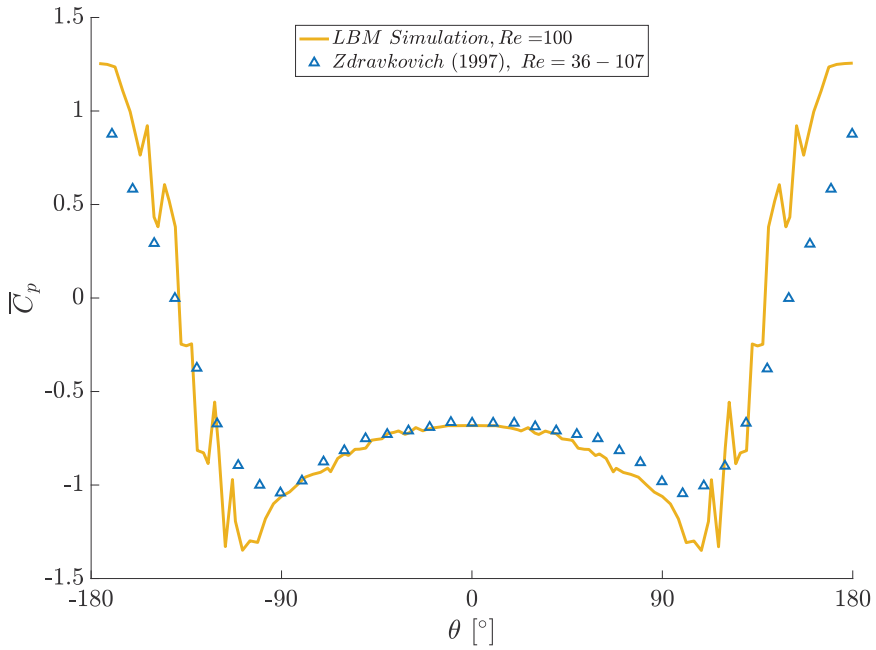

Figure 9: Time-averaged pressure coefficient distribution $\bar{C}_p(\theta)$ on the surface of a circular cylinder at $Re_D = 100$. Results from the present LBM simulation are compared with experimental data by Zdravkovich (1997).

coefficient is observed, with the trend being well captured by the LBM results. Yet, at the LE region ($\theta = \pm 180°$), the LBM results demonstrate higher $\bar{C}_p$ values than the experimental data, likely attributable to a difference in the Reynolds number. One may note that the $\bar{C}_p$ distribution computed from the LBM simulation exhibits various "peaks" around the cylinder surface. These "peaks" are associated with the mesh resolution selected for the circular cylinder. Since a Cartesian mesh with uniform spacing between all nodes was utilized for this LBM simulation, inaccuracies are likely to occur when applied to an obstacle with rounded boundaries. Enhancing the mesh resolution can help reduce such inaccuracies. Given that the primary geometry to be investigated in this study (double-cavity) does not include rounded boundaries, a more advanced solid boundary condition will not be implemented in this context.

The time-varying integral lift ($C_L(t)$) and drag ($C_D(t)$) force coefficients are analyzed below to provide further insights into the vortex-shedding phenomenon. Such analysis can also help identify whether the artificial "peaks" shown in Fig. 9 influence the accuracy of the LBM solver in capturing the unsteady characteristics. The instantaneous integral lift and drag force coefficients are derived by integrating the pressure coefficient distribution on the cylinder's surface at each iteration. This process simulates each node as a small panel subjected to a given pressure, assuming all panels are similar in length. By summing the pressure contribution from each panel while accounting for its

orientation and length, the overall forces along the x and y axes can be calculated as follows:

$$\begin{aligned} C_L &= -\sum_{i=1}^{N} C_{p_i} \cdot l \cdot \sin(\theta_i), \\ C_D &= -\sum_{i=1}^{N} C_{p_i} \cdot l \cdot \cos(\theta_i), \end{aligned} \tag{27}$$

where N is the number of panels, C_{p_i} and θ_i are the pressure coefficient and the orientation angle at panel i respectively, and l is the normalized panel length (by D). This way, the instantaneous lift and drag coefficient can be computed at each iteration, as presented in Fig. 10.

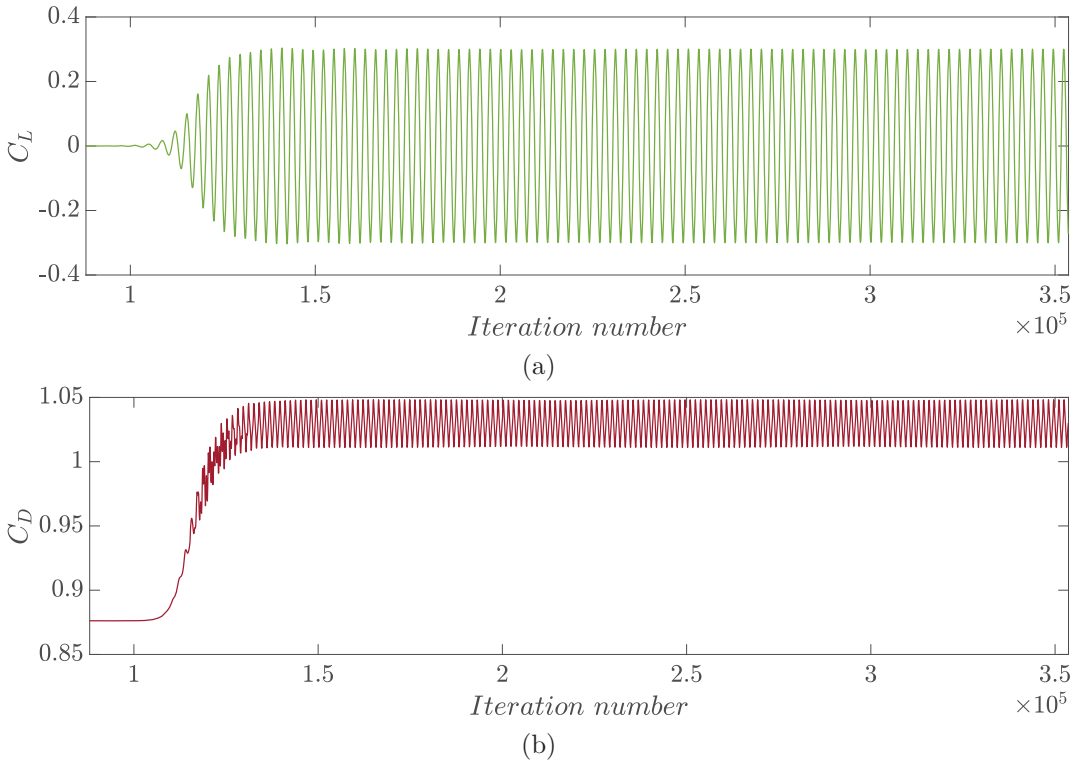

Figure 10: Time history of the lift (C_L) and drag (C_D) coefficients for a circular cylinder at $Re_D = 100$, as obtained from the LBM simulation. (a) Lift coefficient. (b) Drag coefficient.

As shown in Fig. 10, the lift coefficient exhibits fluctuations centered around zero, with peaks ranging from -0.3 to 0.3, while the drag coefficient exhibits fluctuations around 1.03, with peaks ranging from 1.05 to 1.01. Based on the time-varying lift and drag coefficient results, the LBM simulation reaches a quasi-steady state after 150,000 iterations, which is characterized by the cylinder shedding vortices at a constant rate. At the quasi-steady state, one can analyze several flow characteristics and compare them to previously published results. Firstly, the mean values of the lift and drag coefficients ($\overline{C}_L$ and $\overline{C}_D$) are computed, as well as the fluctuations of these coefficients (C'_L and C'_D) and compared to the results of Zdravkovich (1990).

The mean lift coefficient is documented with precision as it is intended to be (zero), whereas $\overline{C}_D$, C'_L, and C'_D demonstrate certain deviations in comparison to Zdravkovich (1990) for similar

	LBM simulation	**Zdravkovich (1990)**
$\overline{C}_L$	0	0
C'_L	0.3	0.1
$\overline{C}_D$	1.03	1.4
C'_D	0.02	0

Table 2: Comparison of $\overline{C}_L$, $\overline{C}_D$, C'_L and C'_D between the LBM simulation and Zdravkovich (1990).

Reynolds number.

Secondly, the Power Spectral Density (PSD) spectrum of the lift coefficient signal can be analyzed to identify the dominant fluctuation frequency in the quasi-steady state. This, in turn, allows for determining the Strouhal number (St) associated with the vortex shedding and oscillating flow mechanisms in general. Here, we will examine the Strouhal number based on the diameter of the cylinder, defined as $St_D = fD/U_\infty$.

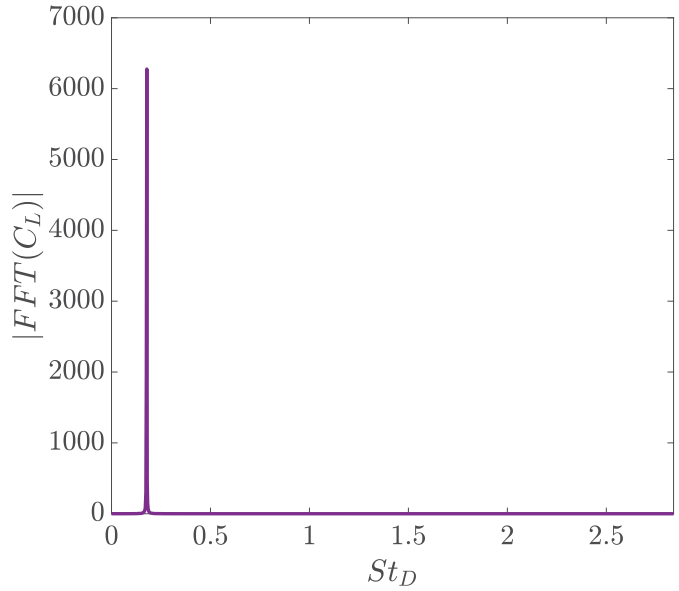

Figure 11: PSD of the lift coefficient (C_L) signal for a circular cylinder at $Re_D = 100$, plotted against the Strouhal number based on cylinder diameter.

Fig. 11 shows the PSD of the lift coefficient (C_L) signal, highlighting the predominant frequency of the lift coefficient oscillation, which indicates the Strouhal number associated with the vortex shedding is $St_D = 0.178$. The resulting vortex-shedding Strouhal number for a circular cylinder at $Re_D = 100$ exhibits similarities to numerous previous studies, including Lienhard et al. (1966) and Norberg (2001) where the Strouhal number is $St_D = 0.165$.

This section aimed to validate the in-house LBM code algorithm against a generic case of uniform flow around a circular cylinder at a Reynolds number of $Re_D = 100$. The LBM results obtained agree with previously established results from similar studies. However, some deviations exist, particularly concerning "peaks" in the pressure distribution on the cylinder surface around the leading edge region. It has been concluded that such deviations are likely attributable to the grid resolution and the rounded boundaries of the tested obstacle. Consequently, rounded bodies are generally less

appropriate for the bounce-back boundary condition, which is more effective when used on obstacles with sharp edges. This study aims to study the flow characteristics in a double-cavity configuration, which is characterized merely by sharp edges; therefore, the bounce-back boundary condition will still be used in the following sections. To validate the LBM algorithm against a case more analogous to the primary case (double-cavity), a secondary validation case involving the flow around a two-dimensional square within a channel will be studied. Following this approach will allow one to confirm that the errors encountered with the circular cylinder case are eliminated in a geometry characterized by sharp edges, as anticipated. Furthermore, an initial validation of the channel flow algorithm will be achieved, which will subsequently be applied to the primary case.

3.1.2 2D laminar flow over a square cylinder in a channel

This validation case has been generated to provide an initial insight into the Poiseuille flow field within the LBM algorithm and to thoroughly validate the precision of the bounce-back boundary condition on obstacles with straight-edged boundaries. This will be achieved by solving the case of a two-dimensional flow field surrounding a square placed at the center of a channel. The LBM results obtained here will be validated against previously published results of the same case by Breuer et al. (2000) and Zhou et al. (2005). To ensure an accurate comparison as possible, the size of the computational domain investigated here was kept similar to those in previous studies.

Figure 12: Computational domain of the two-dimensional square in a channel.

The domain characterized by the square side length D exhibits similarities to the circular domain referenced in the previous case, as depicted in Fig. 12. Three primary dimensions determine both the size of the domain and the positioning of the square within it. The first is the domain length, which measures $50D$; the second is the channel width, set to $8D$. Furthermore, the square's center is positioned at the mid-width of the channel, at a distance of $12.5D$ from the inlet. This computational domain closely resembles the domains utilized in the comparative studies, aiming to effectively capture a sufficient number of shed vortices while minimizing reflections from the outlet boundary, similar to the previous validation case.

The simulation was conducted using the BGK collision model and employing a Poiseuille flow in a channel, which enforces a fully developed parabolic velocity profile at the inlet, as detailed in section 2.5 and illustrated in Fig. 13b. The peak velocity of the inlet profile is set to $U_\infty^{max} = 0.1$ [node/iteration], analogous to the uniform flow velocity observed in the previous case. The square side length was set to $D = 40$ [nodes], and consequently, the entire domain mesh was prescribed according to this resolution, as illustrated in Fig. 12. The Reynolds number is defined based on the square side length, Re_D. The LBM solver was used to simulate the configuration above at various values of Re_D, specifically $Re_D = [10, 50, 100, 150, 200, 250]$. The results obtained from each simulation are compared to those reported in the reference studies. One of the goals of this validation case is to analyze the normalized velocity magnitude field ($\frac{|\vec{u}|}{U_\infty^{max}}$) as well as the normalized vorticity magnitude field ($\frac{|\vec{\omega}|}{U_\infty^{max}/D}$) such as the previous case. Furthermore, the ability of the LBM solver to accurately capture the vortex-shedding phenomenon behind the square will be assessed.

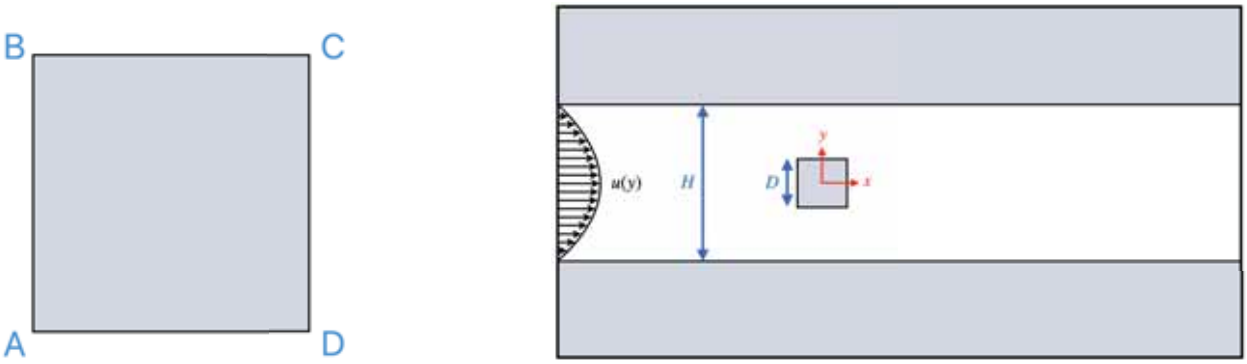

(a) (b)

Figure 13: (a) The square and its corresponding point are arranged in accordance with the established order. (b) The square positioned within the channel exhibits the fully developed parabolic velocity profile at the designated inlet location.

Fig. 14 and Fig. 15 show the effect of the Reynolds number on the instantaneous flow field around the square in terms of the velocity magnitude and the vorticity magnitude contours. The fully developed Poiseuille velocity profile is successfully enforced at the inlet, thus enabling an accurate representation of the boundary layer along the wall, as illustrated in Fig. 14. It is important to note that the vorticity of the boundary layer is not observed in Fig. 15, as the magnitude of the vorticity in this region is significantly smaller than that of the shed vortices. The vortices shed behind the square are captured in both Fig. 14 and Fig. 15. Increasing the Reynolds number causes the vortices to shed over longer distances at the same given time instance (iteration) before they weaken. For Reynolds numbers of $Re_D = 10$ and $Re_D = 50$, the Reynolds number is below a critical threshold, resulting in the absence of a vortex street behind the square.

In addition to analyzing the instantaneous flow field of the square across all simulated regimes, it is imperative to examine the results temporally. This procedure will be performed similarly to the prior validation case, in which the mean pressure distribution over the surface of the obstacle will be compared to previously published results. The instantaneous pressure coefficient is calculated in the same manner as described in Eq. (26), progressing sequentially from vertex A to vertices B, C, and D, as illustrated in Fig. 13a. In the study conducted by Zhou et al. (2005), the time-averaged pressure coefficient was computed for a Reynolds number of $Re_D = 250$, to which the corresponding LBM results will be compared.

Figure Fig. 16 shows the time-averaged pressure distribution on the square surface, depicting a good agreement between the LBM results and the reference results published by Zhou et al. (2005). On the front side of the square (AB), the mean pressure coefficient aligns closely, except for a minor deviation noted at the middle zone of the side. Minor inconsistencies are observed in the top and bottom sections (BC and AD, respectively). A highly favorable agreement is noted for the bottom section, whereas a minor deviation is present in the top section.

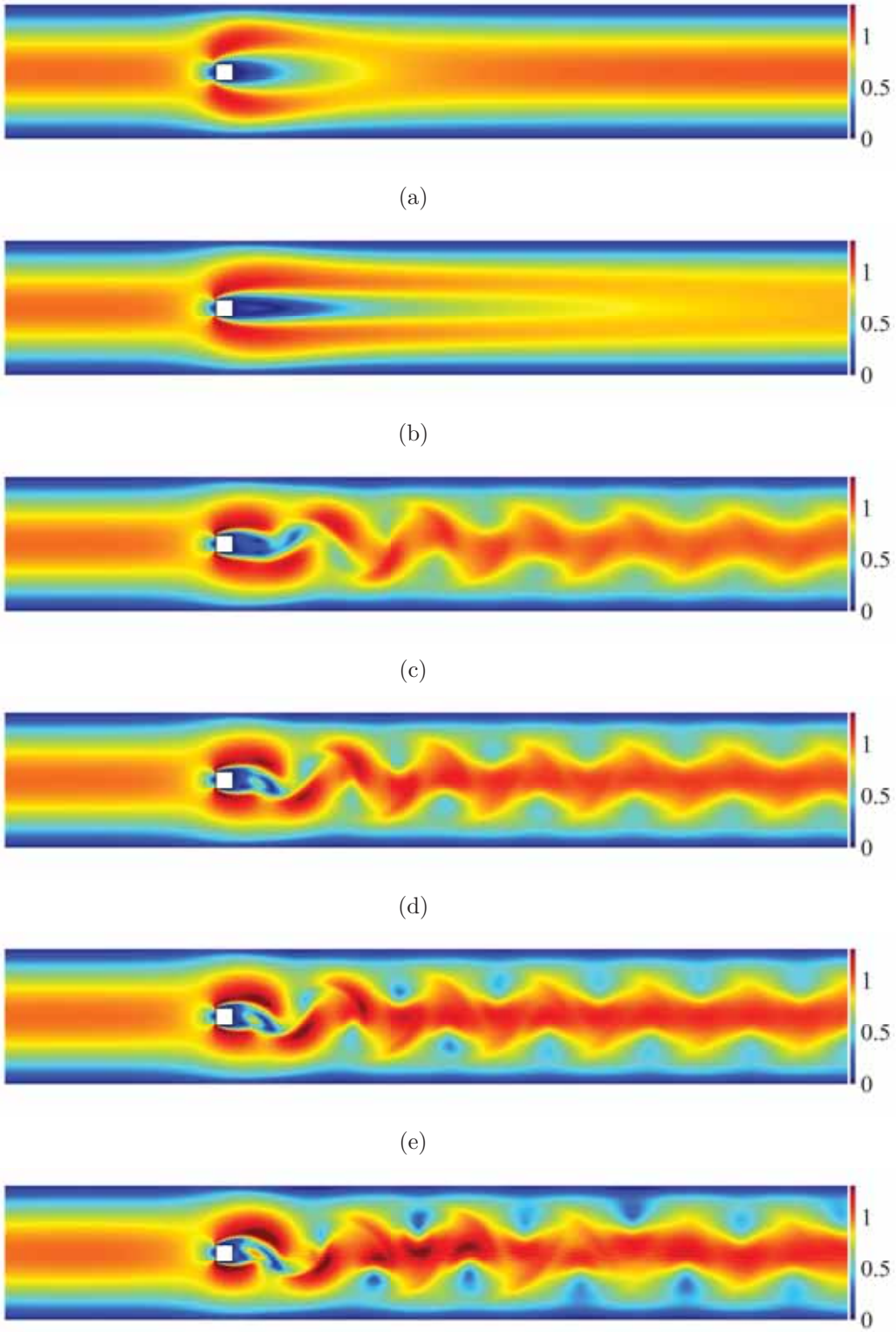

Figure 14: Instantaneous flow field of the normalized velocity magnitude around a square obstacle within a channel (iteration 200,000). The velocity magnitude is normalized by the maximum freestream velocity, $|\vec{u}|/U_{\infty}^{\max}$. (a) $Re_D = 10$; (b) $Re_D = 50$; (c) $Re_D = 100$; (d) $Re_D = 150$; (e) $Re_D = 200$; (f) $Re_D = 250$.

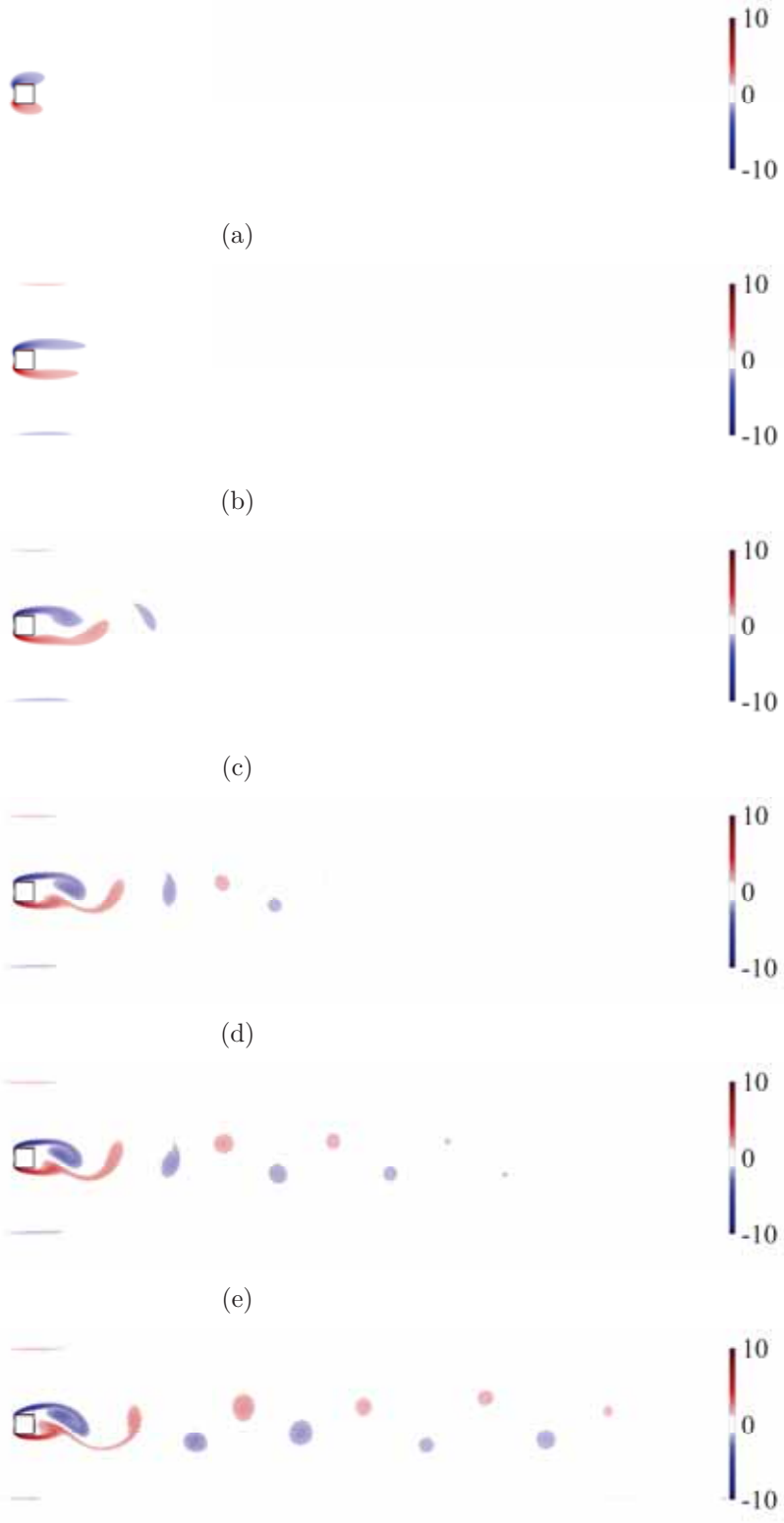

Figure 15: Instantaneous flow field of the normalized vorticity magnitude around a square obstacle within a channel (iteration 200,000). The vorticity is normalized by the maximum freestream velocity and the square side length, $|\vec{\omega}|D/U_{\infty}^{max}$. (a) $Re_D = 10$; (b) $Re_D = 50$; (c) $Re_D = 100$; (d) $Re_D = 150$; (e) $Re_D = 200$; (f) $Re_D = 250$.

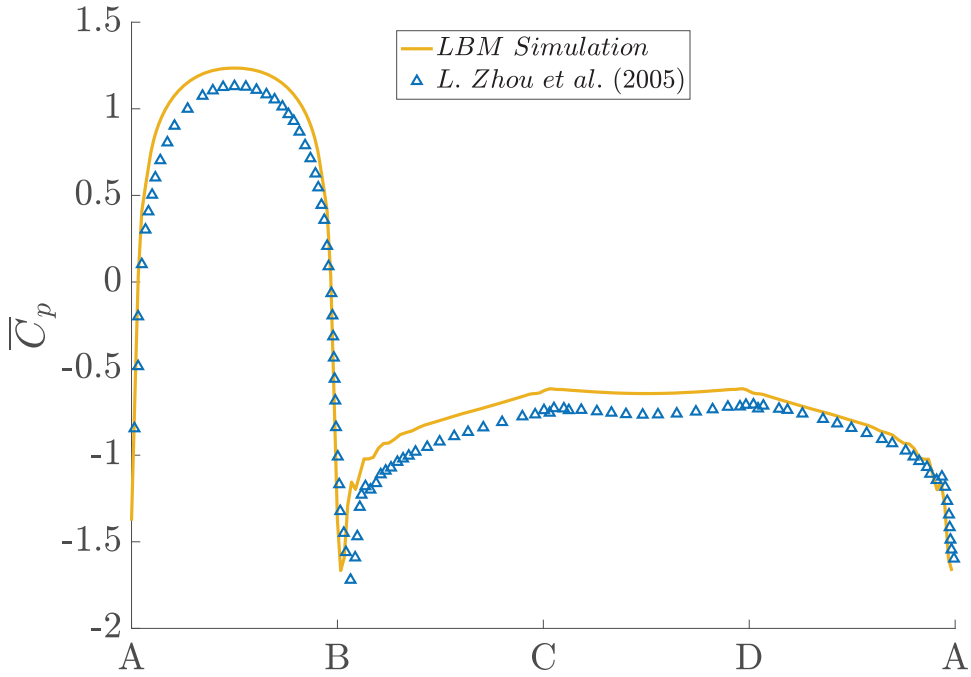

Figure 16: The time-averaged pressure coefficient distribution $\bar{C}_p$ on the surface of a square at $Re_D = 250$. Results from the present LBM simulation are compared with the data results reported by Zhou et al. (2005).

To facilitate a more profound analysis and comparison of the results, as well as to ensure that the unsteady flow characteristics are consistent with the Reynolds number, the mean drag coefficient ($\overline{C}_D$) and the vortex-shedding Strouhal number derived from the instantaneous lift coefficient signal are computed for each flow regime. The numerical results are compared with existing published results to validate the LBM algorithm. The instantaneous signals of the lift and drag coefficients are computed from Eq. (27), under the same assumptions, where the orientation angle of the surface θ_i will be 180° for AB side, 90° for BC side, 0° for CD side and 270° for AD side. The vortex-shedding Strouhal number is identified from the PSD spectrum of the lift coefficient signal, computed as $St_D = fD/U_\infty^{max}$.

As shown in Fig. 17, an excellent agreement is observed between the LBM results and the reference studies for both the mean drag coefficient and the Strouhal number across nearly all flow regimes. In Fig. 17a, for $Re_D > 100$, the mean drag coefficient is notably similar across all three studies. Conversely, for Reynolds numbers 10 and 50, a significant difference is evident between all data sets, which increases as the Reynolds number decreases. Generally, the mean drag coefficient increases as the Reynolds number deviates from the range between 100 and 150. This increase in the mean drag coefficient is markedly sharper when the Reynolds number decreases rather than increases. In Fig. 17b, the results for $Re_D = 50$ and $Re_D = 10$ are not presented since the vortex shedding phenomenon behind the square was not observed for such small Reynolds numbers. These flow regimes fall below the critical threshold at which a laminar vortex street begins to develop, as illustrated in Fig. 14 and Fig. 15. As the Reynolds number diverges from $Re_D = 150$, where the variance between the LBM and the reference results is most pronounced, the Strouhal values become

increasingly comparable between data sets. Overall, the Strouhal number reaches its maximum value at $Re_D = 150$ among the four Reynolds numbers analyzed. As the Reynolds number deviates from this point, the Strouhal number decreases.

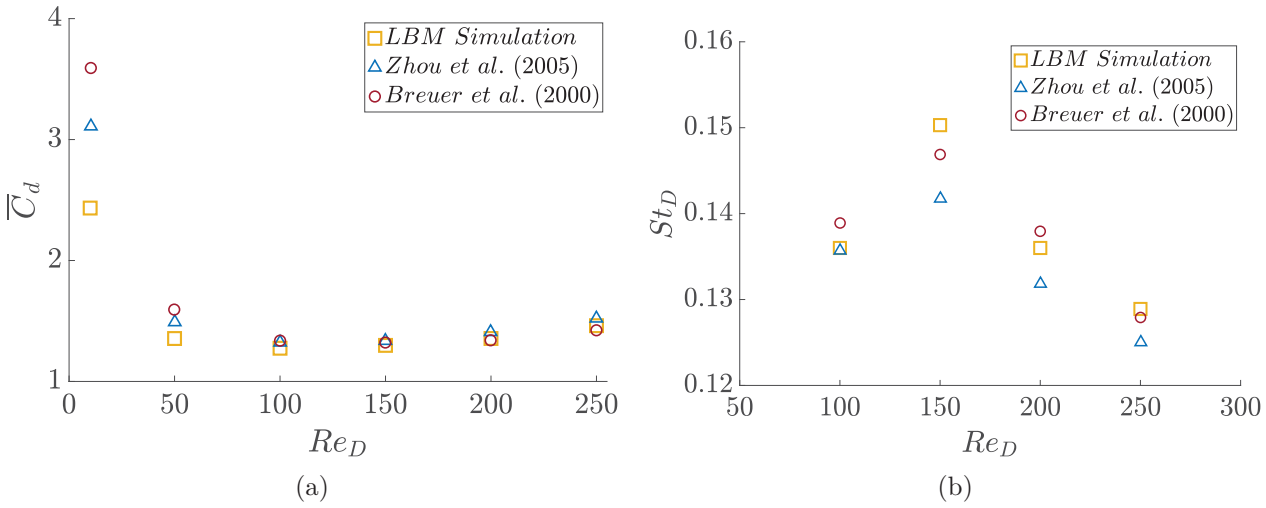

Figure 17: Comparison of current LBM results (□) with previously published results from Zhou et al. (2005) (△) and Breuer et al. (2000) (○) as a function of the Reynolds number Re_D. (a) Time-averaged drag coefficient ($\overline{C}_D$). (b) Strouhal number (St_D).

To summarize, this section presents a validation of the in-house LBM code algorithm by employing a different case from the initial one, which meets new objectives: i) application of the BB boundary condition on an obstacle featuring straight surfaces, and ii) initial implementation of the Poiseuille boundary condition to simulate fully developed flow within a channel. Overall, the LBM results obtained are in good agreement with those presented by Breuer et al. (2000) and Zhou et al. (2005). Consequently, the in-house LBM solver can be used to simulate and analyze the primary case study, namely the double-cavity configuration, with increased confidence.

3.2 Simulation results for a double-cavity configuration in a channel

With the LBM algorithm validated with canonical cases, it is now possible to solve the primary case of a double-cavity in a channel and compare the results with previously published findings by Tuerke (2017). The main flow phenomena to be resolved in the double-cavity configuration are the shear layer oscillations and the vortex development in the cavity. Those will be analyzed both in time and frequency domains. A specific non-dimensional configuration of the double cavity will be examined, and the changes in the flow regime will be analyzed as a function of varying Reynolds numbers under this setup.

The examined double-cavity configuration is characterized by the dimensions presented in Fig. 1. For this configuration, the cavity length (L) is used as the domain resolution scale, defined as $L = 400$ [nodes], which characterizes all other dimensions. This resolution value was selected as it yielded sufficient accuracy with relatively fast runtime. The studied configuration is characterized by a cavity length-to-depth ratio of $L/H = 2$ and a channel height of $D = 0.2L$. In addition, to reduce the effects of reflective waves from the inlet and outlet boundaries, the upstream and downstream channel lengths are set at $L_1, L_2 = 2.4L$, as illustrated in Fig. 18.

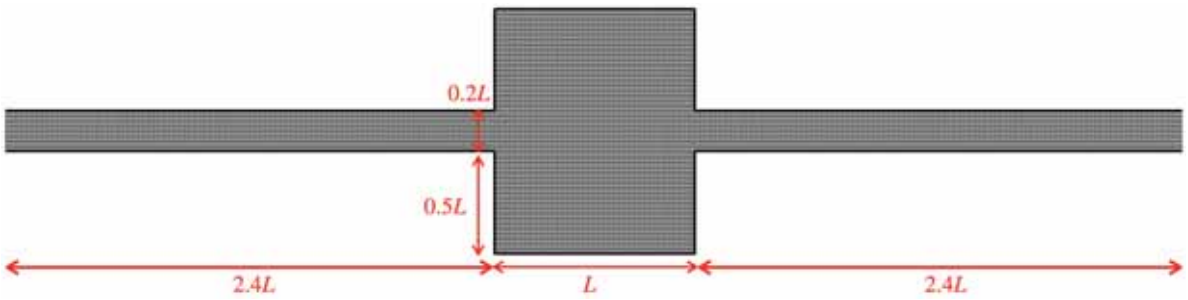

Figure 18: Double cavity, two-dimensional domain.

LBM simulations of the double-cavity configuration were executed utilizing the TRT collision model for improved numerical stability and implementing a Poiseuille flow within a channel. This configuration enforces a fully developed velocity profile at the inlet, as delineated in section 2.5 and illustrated in Fig. 1. The peak velocity of the inlet profile is $U_{\infty}^{max} = 0.1$ [node/iteration], similar to the velocity profile in section 3.1.2. The definition of the cavity length-based Reynolds number Re_L is described in section 1. In this discussion, simulations are examined for different values of Re_L, (3600, 5100, 7000, and 10000) to study four different flow regimes in the double-cavity configuration. Due to the generation of waves that reflect from the inlet and outlet boundaries into the double-cavity region, adversely affecting the flow field results, the characteristics boundary condition (CBC) is applied as a non-reflective boundary condition at both the inlet and outlet boundaries. In addition, a buffer zone, often referred to as a 'sponge layer', is also implemented, as detailed in section 2.5.

To adequately analyze the flow field results within the double cavity over time, eight probes were strategically positioned within the cavities to record the horizontal and vertical velocities of the fluid throughout the entire simulation runtime. The positions of the probes were selected according to Tuerke (2017), as illustrated in Fig. 19. Probes P_1 to P_5 are designated positions oriented in the same x-direction, situated at 85% of the cavity length from the cavity leading-edge. Specifically, P_1 and P_5 correspond to locations at half the depth of the bottom and top cavities, respectively, P_2

and P_4 are located at the edges of the bottom and top cavities, respectively, while P_3 is positioned in the center of the channel. Furthermore, points P_6 and P_7 are designated positioned along the x-direction, located at 60% of the cavity length. P_6 is situated at half the depth of the bottom cavity, whereas the P_7 position is at the edge of the bottom cavity. P_8 is positioned at 35% of the cavity length in the x-direction and at half the depth of the bottom cavity in the y-direction. All probes recorded the velocity signal at each iteration, indicating a non-dimensional sampling frequency of 1 [1/iteration].

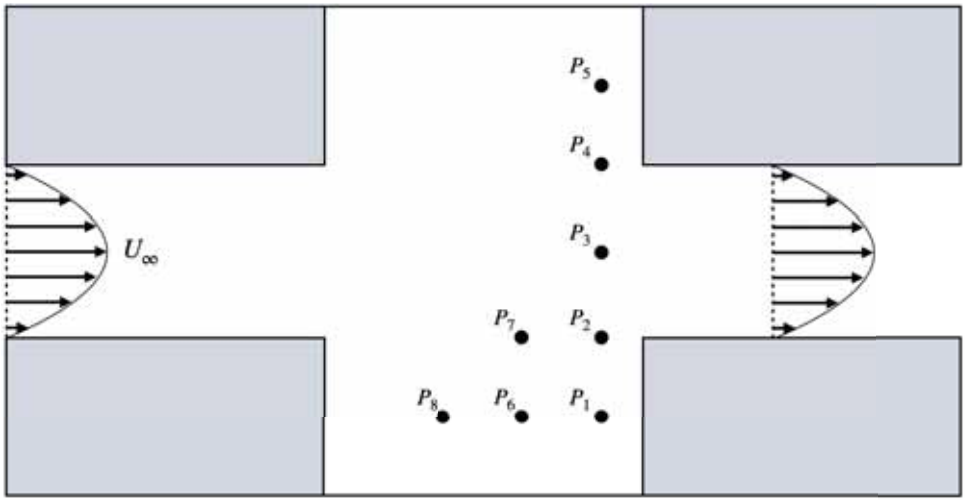

Figure 19: Probes locations in the double cavity computational domain.

Similar to the validation cases, this study will present and analyze the normalized velocity magnitude field ($\frac{|\vec{u}|}{U_\infty^{max}}$) and the normalized vorticity field ($\frac{|\vec{\omega}|}{U_\infty^{max}/D}$) within the context of the double cavity configuration. Fig. 20 and Fig. 21 show instantaneous flow field results for different Reynolds numbers, as computed from the LBM simulations, showing four distinct flow regimes. The resultant flow fields for Reynolds numbers 3600, 5100, 7000, and 10000 were categorized into steady, periodic, intermediate, and chaotic flow regimes, respectively. The periodic regime, observed at a Reynolds number of 5100 (see Fig. 20b and Fig. 21b), exhibits several anticipated and distinctly defined phenomena. These phenomena will be thoroughly examined in this section, and based on these observations, a comprehensive understanding of the flow physics in the double-cavity configuration will be obtained. For all flow regimes, a fully developed laminar flow is shown in the inlet channel. In this channel, the boundary layers do not change in thickness or experience further development along the channel; instead, they remain at their maximum thickness in a steady state. This observation confirms the effectiveness of the boundary conditions implemented for this particular flow type. In the region of the double cavity, particularly in the steady and periodic flow regimes (see Fig. 20a, Fig. 21a, Fig. 20b and Fig. 21b), two large vortices (primary re-circulation regions) with diameters occupying almost the entire depth of each cavity are observed, rotating in opposite directions. These vortices are located at the rear part of the cavities, near the back wall. The vortices in the cavities are surrounded by a set of additional vortex structures rotating in the opposite direction to the primary vortex they encircle. This phenomenon, involving two large vortices (one in each cavity) surrounded by smaller counter-rotating vortices, is expected for this configuration and is schematically illustrated in Fig. 1, as described in Tuerke (2017). The oscillatory motion of

the shear layers is an additional phenomenon observed within the cavity region across all regimes but the steady regime. When the fully developed boundary layers from the channel enter the cavity region, where the channel walls suddenly expand, they transform into shear layers that propagate downstream. At some streamwise position along the cavity length, the shear layers lose stability and start oscillating in a wavy manner at a characteristic frequency. This instability arises due to the influence of the primary vortices formed in the cavities and fluid reflections caused by the presence of the cavities. The shear layer oscillations occur at a constant rate and in a synchronized manner between the two cavities, with their effect visible in the downstream channel. In the downstream channel, such oscillations promote the formation of a flow profile that varies in both time and space, resulting in non-uniform and underdeveloped boundary layers in the initial segment of the channel. It is only after a requisite progression of fluid through the channel that these oscillations achieve stabilization, thereby facilitating the formation of a steady and uniform flow profile that corresponds with the fully developed flow conditions imposed in the boundary conditions and illustrated in the upstream channel. Apart from these primary phenomena, the velocity magnitude field indicates the formation of two additional vortices at the front section of the cavities, which are approximately equivalent in size to the primary vortices. However, these vortices exhibit significantly lower strength in comparison to the primary vortices, making them indiscernible in all flow regimes except for the $Re_L = 10000$. In addition to the phenomena occurring within the periodic flow field, Fig. 20c and Fig. 21c illustrate that the periodicity begins to diminish in the intermediate flow regime. This is evident from the more circular shape of the two primary vortices compared to their shape in the periodic regime. Moreover, the thickness of the vortex structures surrounding the primary vortices varies. Also, the magnitude of the shear layer oscillations is considerably greater, necessitating an extended downstream distance within the channel before a stable velocity profile indicative of fully developed flow is established. In the chaotic flow field illustrated in Fig. 20d and Fig. 21d, the distinct structure of the two primary vortices breaks down, resulting in the loss of coherence for both the primary vortices and their surrounding vortex structures. Furthermore, the vortices located at the front section of the cavities have strengthened, making them more distinguishable, though they, too, have lost coherence. In the downstream channel, an increased distance is now necessitated for the velocity profile to attain stabilization and achieve a fully developed flow state.

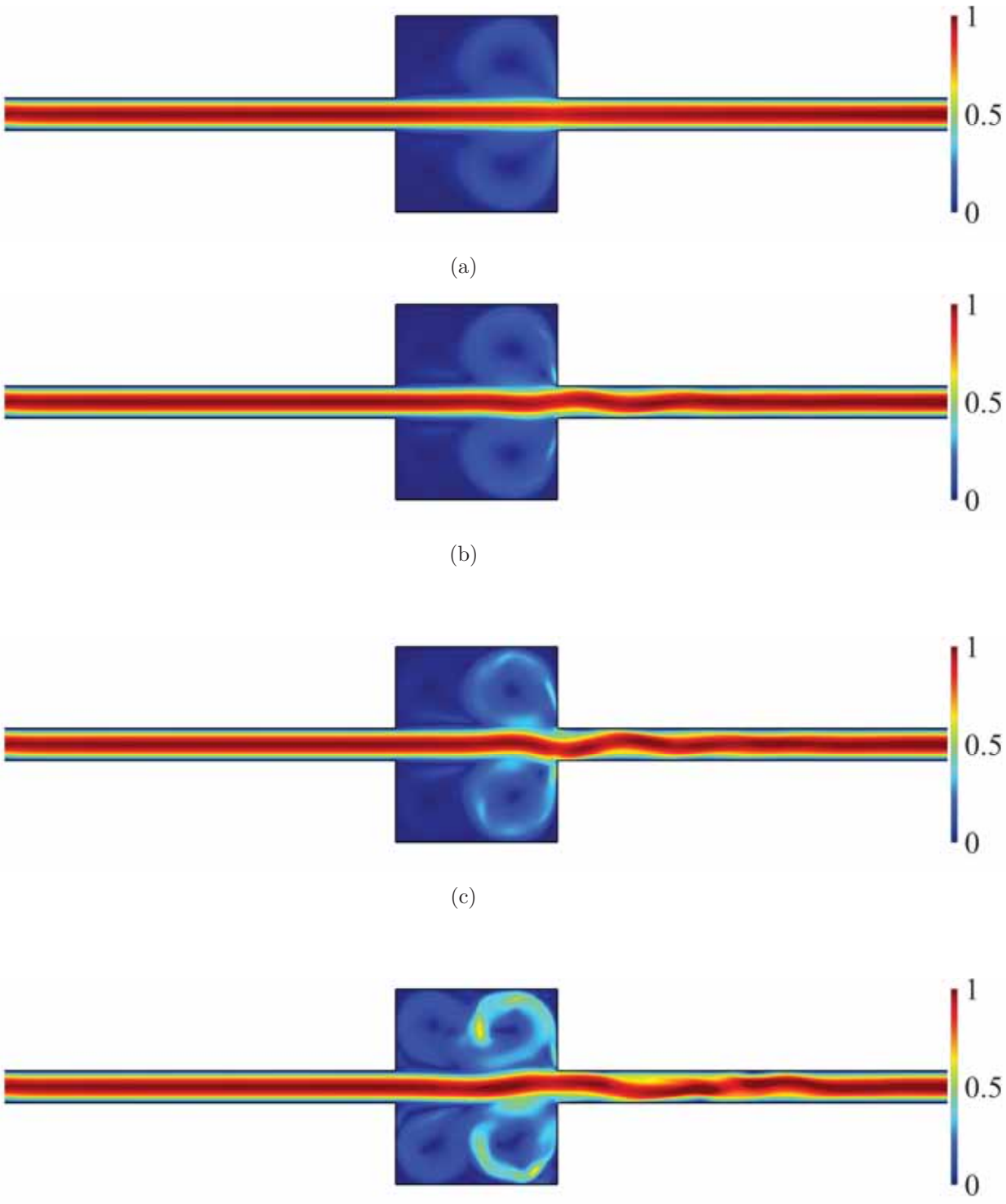

Figure 20: Instantaneous flow field of normalized velocity magnitude in a double cavity configuration (iteration 400,000). The velocity magnitude is normalized by the maximum freestream velocity, $\frac{|\vec{u}|}{U_{\infty}^{\max}}$. (a) $Re_L = 3600$, (b) $Re_L = 5100$, (c) $Re_L = 7000$, (d) $Re_L = 10000$.

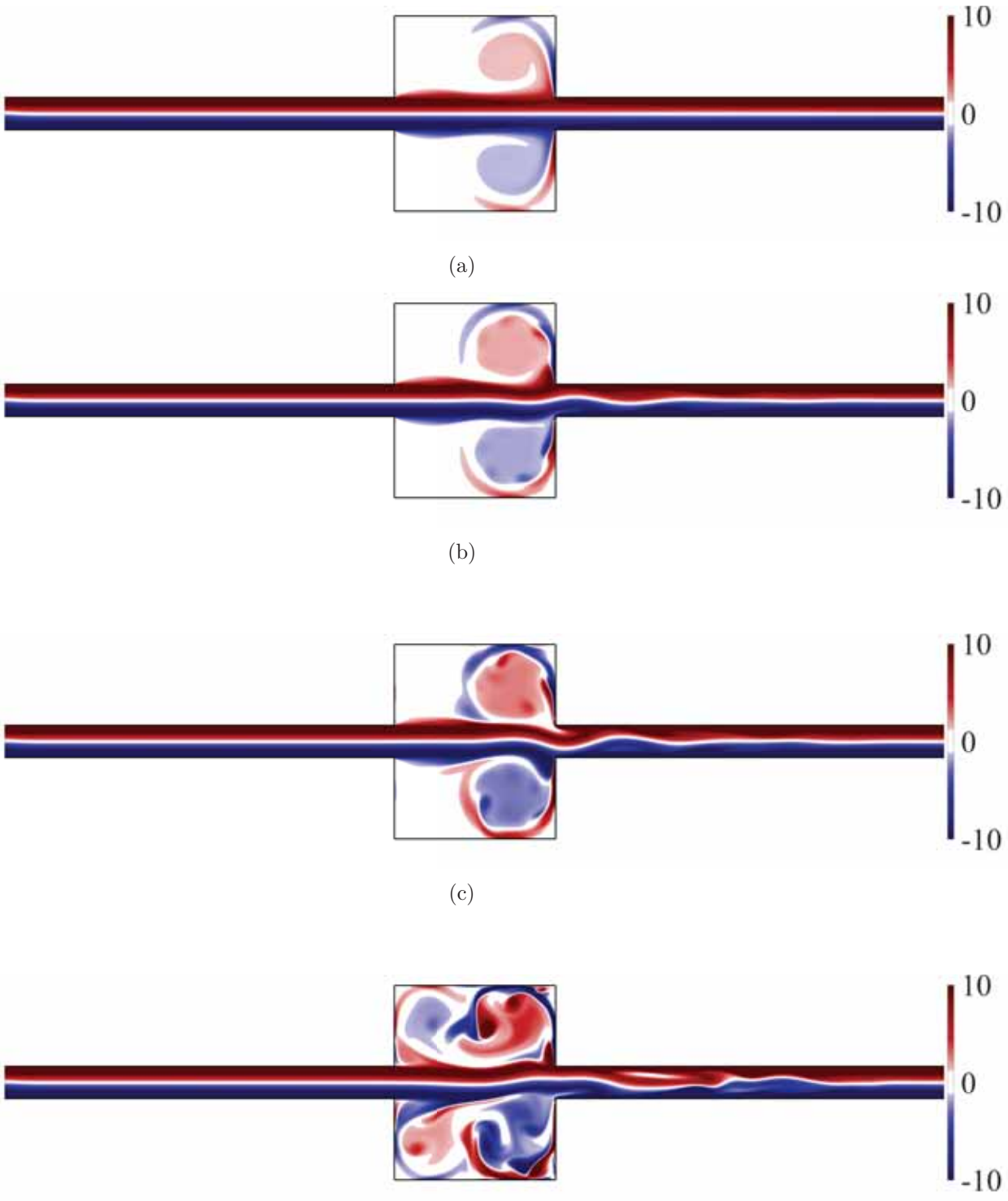

Figure 21: Instantaneous flow field of normalized vorticity magnitude in a double cavity configuration (iteration 400,000). The vorticity is normalized by the maximum freestream velocity, $\frac{|\vec{\omega}|}{U_{\infty}^{\max}/L}$. (a) $Re_L = 3600$, (b) $Re_L = 5100$, (c) $Re_L = 7000$, (d) $Re_L = 10000$.

The simulation performed at a Reynolds number of $Re_L = 5100$ yielded a distinct periodic flow regime, which can be deeply analyzed using all the probes that record the horizontal and vertical velocities, as illustrated in Fig. 19. To further study and validate the results of this flow regime, the signal of the horizontal velocity of each probe is presented, and an FFT spectral analysis is conducted on each probe. This analysis is somewhat similar to the spectral analysis conducted in both validation cases (section 3.1.1 and section 3.1.2). The Strouhal number (St_L) achieved from the spectral analysis is defined as described in section 1. In this manner, eight signals and spectral analysis are obtained, as presented in Fig. 22 and Fig. 23.

The results obtained from the probes successfully capture several key phenomena that characterize the flow within a double cavity situated in a channel, as visually represented in the flow field depicted in Fig. 20b and Fig. 21b. As shown above, two primary vortices (re-circulation regions) appear in the rear part of the cavities (downstream direction). Furthermore, in the overlapping channel region between the cavities, the shear layers seem to oscillate at a specific frequency. The characteristic frequency of the primary vortices and shear layer can be determined by analyzing the spectral data from each probe. The probes positioned at half the depth of a cavity (P_1, P_5, P_6, P_8) captured a single dominant frequency with a Strouhal number of $St = 0.76$, as shown in Fig. 22a, Fig. 22e, Fig. 23a, and Fig. 23c. Based on the probe locations, it can be inferred that this Strouhal number ($St = 0.76$) is indicative of the primary vortex rotation rate frequency, hereafter referred to as St_V (the vortex Strouhal number). The observation that the frequency recorded by probe P_5 is consistent with those obtained from probes P_1, P_6, and P_8 suggests that both primary vortices (in the two cavities) rotate at the same rate. According to the velocity signal, the vortices rotate with a phase of half-period. In regions sufficiently far from the primary vortices, where their influence is minimal, specifically at probe P_3, a different dominant frequency is observed in Fig. 22c with Strouhal number of $St = 1.56$. This Strouhal number is postulated to be a characteristic of the shear layer oscillations, and thus, it is referred to as St_{SL}. Despite the dominance of the shear layer oscillation frequency at this probe ($P3$), the spectral analysis Fig. 22c indicates a slight influence from the primary vortices in the center of the channel due to the specified channel width. At the probes located at the cavity entrance (P_2, P_4, P_7), a combination of both observed frequencies (St_V and St_{SL}) can be detected. Nevertheless, in this region, the primary vortex Strouhal number St_V appears to be more prominent than the shear layer oscillation Strouhal number St_{SL}. It is noted that the shear layer Strouhal number St_{SL} is identical for similar probes in both cavities (P2 and P4). This observation indicates that akin to the two primary vortices, both shear layers oscillate at the same frequency.

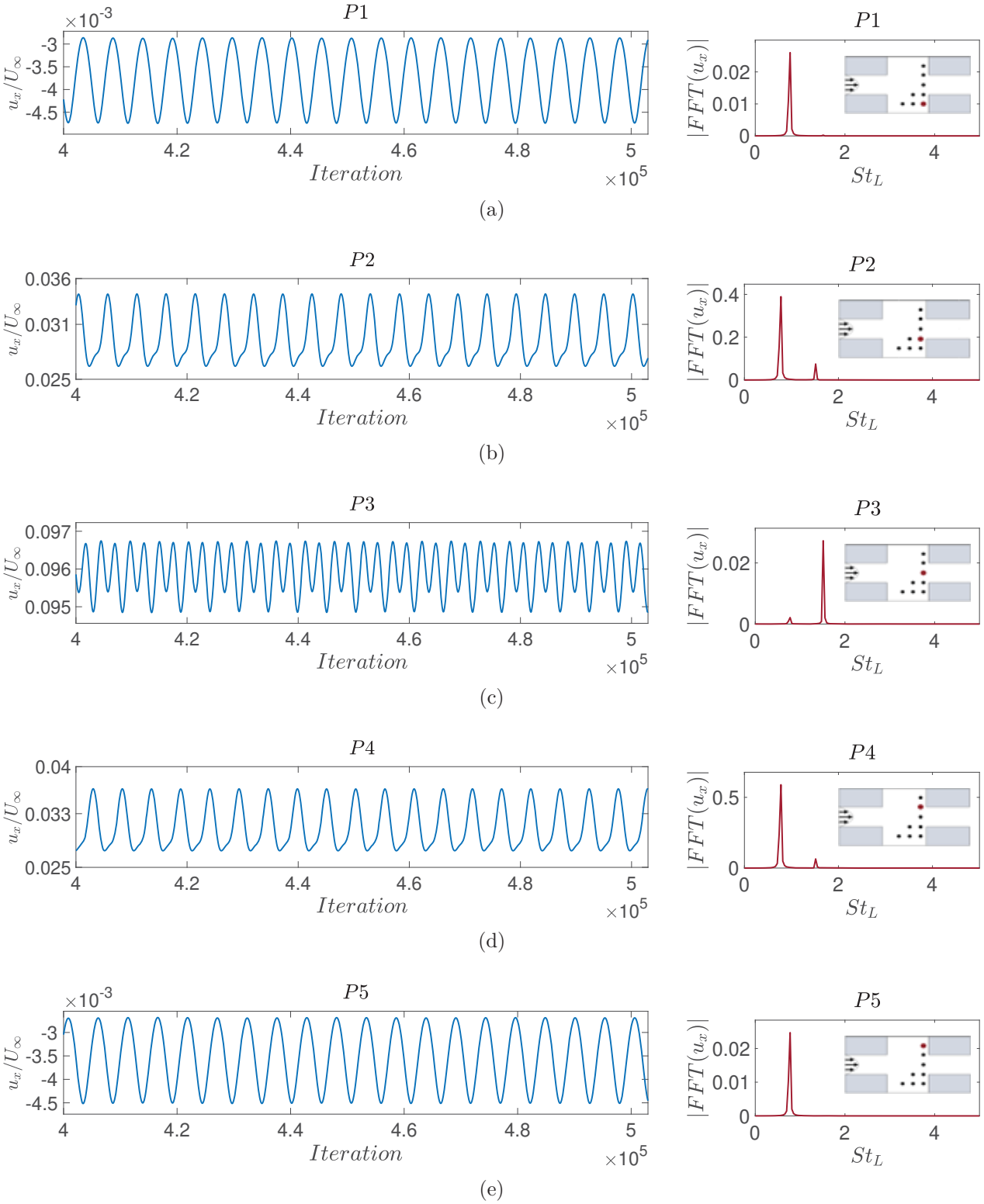

Figure 22: Left - Time-varying signal of the normalized horizontal velocity (u_x/U_∞) recorded at the probes. Right - FFT based on the PSD of the velocity signal from the probe. The data was recorded and taken from the simulation of $Re_L = 5100$. (a) probe P_1. (b) probe P_2. (c) probe P_3. (d) probe P_4. (e) probe P_5.

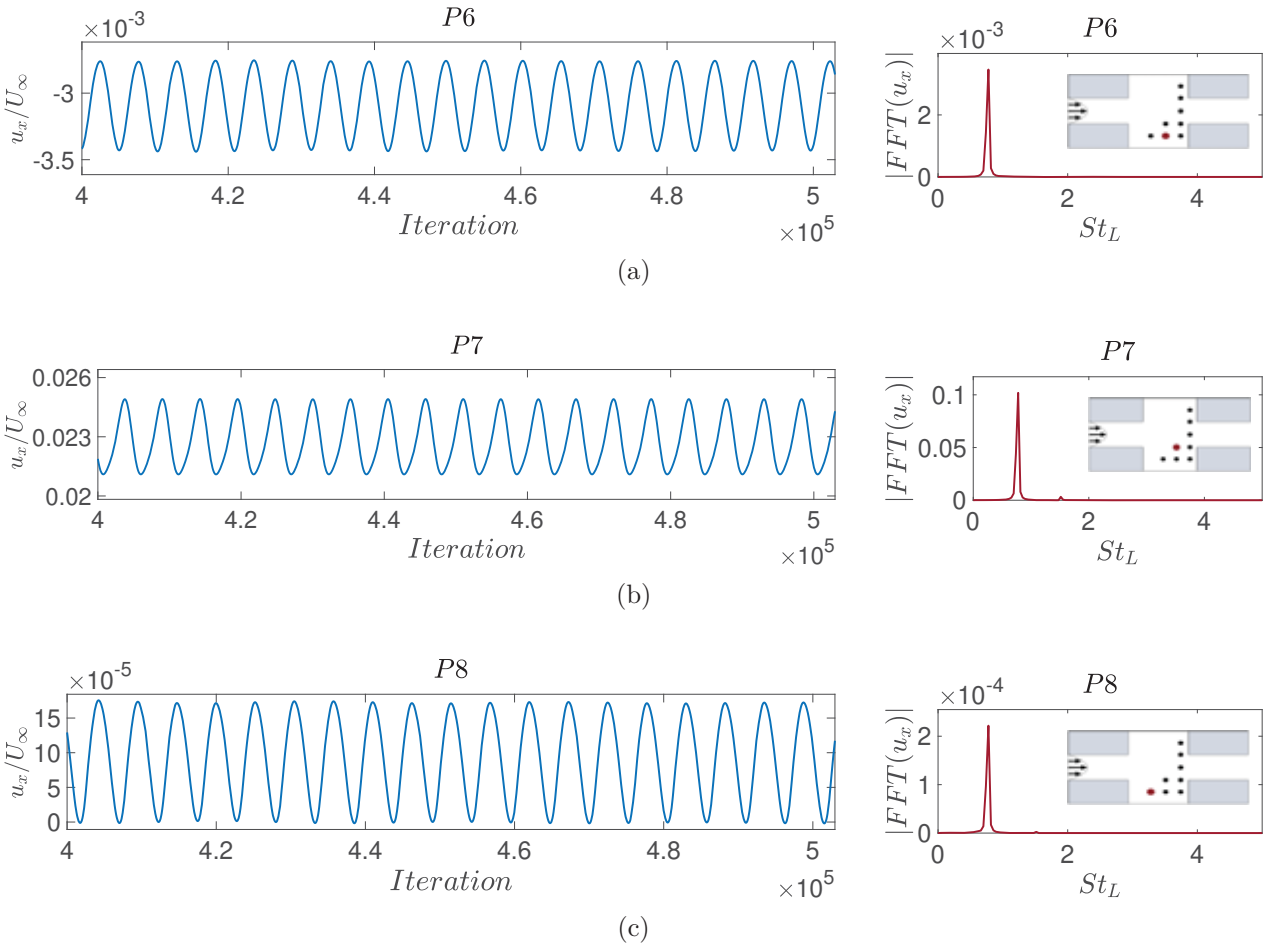

Figure 23: Left - Time-varying signal of the normalized horizontal velocity (u_x/U_∞) recorded at the probes. Right - FFT based on the PSD of the velocity signal from the probe. The data recorded and taken from the simulation of $Re_L = 5100$. (a) probe P_6. (b) probe P_7. (c) probe P_8.

To validate the results obtained, a comparison is presented based on a similar analysis undertaken by Tuerke (2017). In their study, the signals of horizontal velocity were recorded at each of the eight probes, and PSD spectra were computed. This analysis was conducted under identical cavity dimensions ($L/H = 2$ and $D/L = 0.2$) and a similar Reynolds number ($Re_L = 5100$). The simulation results by Tuerke (2017) show a periodic flow regime to evolve within the double-cavity configuration, similar to the LBM results presented here Tuerke (2017). The flow field shown in Fig. 21b appears to be identical to the one obtained by Tuerke (2017) for the same Reynolds number. Tuerke (2017) reported two dominant characteristic frequencies in the spectra of the signals recorded from probes P2, P3, P4, and P7. Within the probes positioned at half the depth of the cavities (P_1, P_5, P_6, P_8), a singular dominant frequency was identified, representing the Strouhal number of the primary vortices with a value of $St_V = 0.88$. It is noteworthy that, in contrast to our findings (see Fig. 23a), Tuerke (2017) identified an additional higher, albeit less dominant, frequency in probe P_6. In the probe positioned at the center of the channel (P_3), Tuerke (2017) identified two dominant Strouhal numbers, which align with our findings. The higher of these Strouhal numbers corresponds to the shear layer oscillation frequency, quantified at a value of the Strouhal number $St_{SL} = 1.75$. Consistent with our observations for this probe, the impact of the primary vortices in the channel's

center was also observed. In the probes located at the cavity opening (P_2, P_4, P_7), both dominant frequencies are present; however, these frequencies exhibit a higher intensity compared to probe P_3, with the vortex Strouhal number St_V being more dominant in this location. Our findings show a similar trend; nevertheless, a significant distinction is that, in our observations, a greater difference is evident between the two peak values of the dominant frequencies across all three probes (P_2, P_3, P_4). Table 3 provides a comparison between the frequencies acquired from the simulations to those reported by Tuerke (2017). Despite the differences between the simulations, comparable Strouhal numbers were achieved between the LBM simulation and the simulation conducted by Tuerke (2017).

	LBM simulation	**Tuerke (2017)**
St_V	0.76	0.88
St_{SL}	1.56	1.75

Table 3: Comparison of the vortex Strouhal number and the shear layer oscillations Strouhal number between the LBM simulation and Tuerke (2017) results for $Re = 5100$.

To further validate the LBM results of the double-cavity case, a comparison is conducted across several Reynolds numbers, specifically 3600, 5100, 7000, and 10000. The objective is to assess whether the LBM solver can accurately capture the distinct flow regimes in the double-cavity geometry. The resulted velocity magnitude and vorticity fields of the four investigated flow regimes are depicted in Fig. 20 and Fig. 21. These results are examined with a singular representative probe P_2. This probe which is situated at the entrance of the lower cavity and at 85% of the cavity's horizontal length in the downstream direction. For each simulation, the time-varying horizontal velocity component signal at the probe is compared, as well as the spectral content of the signal. Fig. 24 presents the comparison of the LBM results obtained across the four different simulations. The results confirm the formation of the four flow regimes. In Fig. 24a, a steady flow regime is evident as fluctuations are absent from the horizontal velocity signal, which results in no spectral content. In Fig. 24b, two distinct dominant frequencies are observed, as anticipated from the periodic flow regime; the lower frequency correlates with the rotational frequency of the primary vortex in the cavity ($St_V = 0.76$), while the higher frequency corresponds to the shear layer oscillation ($St_{SL} = 1.56$). In Fig. 24c, which depicts the results from the intermediate flow regime, additional dominant frequencies appear beyond the two existing ones observed in the periodic flow regime. These results resemble the behavior observed at a lower Reynolds number ($Re_L \approx 5500$) in the study by Tuerke (2017). This discrepancy could arise from the different upstream channel length utilized in the LBM simulation (doubled from the one used by Tuerke (2017)) or from implementing the buffer zone. In Fig. 24d, which depicts the measurements derived from the chaotic flow regime, a clear periodicity is absent in the signal. Indeed, the chaotic flow field characteristics are manifested in the probe measurement results. As a result, no distinct frequencies are detected in the spectral content, which appears noisier than the results obtained for the intermediate flow regime. Additionally, these results closely resemble those reported by Tuerke (2017) for a Reynolds number of $Re_L \approx 6200$, further reinforcing the observation that there is a slight discrepancy between the Reynolds number and the corresponding flow regime in this study compared to Tuerke (2017) findings.

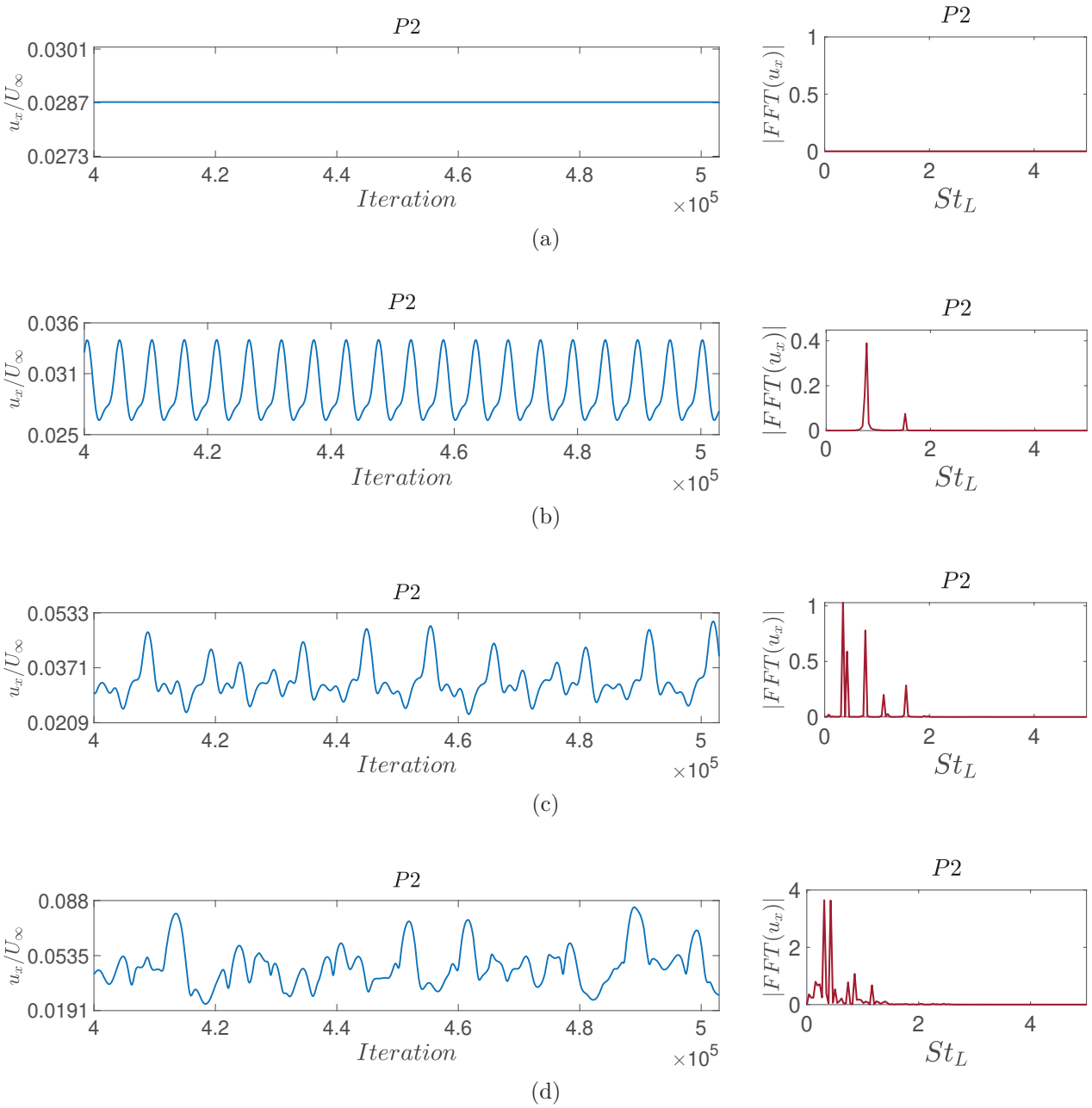

Figure 24: Left - Time-varying signal of the normalized horizontal velocity (u_x/U_∞) recorded at probe P_2. Right - FFT based on the PSD of the velocity signal from the probe. The data was recorded and taken from the simulation of (a) $Re_L = 3600$. (b) $Re_L = 5100$. (c) $Re_L = 7000$. (d) $Re_L = 10000$.

In summery, the performance of the LBM solver was evaluated for a double-cavity configuration. To achieve the above, the LBM results were compared with those published by Tuerke (2017), who utilized an alternative computational method. For a specified double-cavity geometry ($D/L = 0.2$ and $L/H = 2$), the time-varying signal of the horizontal velocity at multiple locations in the flow field was investigated. This approach allowed us to characterize the flow field characteristics in various regions of the cavity. Furthermore, we examined the flow field developed in the double cavity at various Reynolds numbers, chosen to represent different flow regimes. By comparing data derived

from a particular probe, we showed how the flow regimes are reflected in the measurements and identified some discrepancy between the LBM results and the findings reported by Tuerke (2017) for the Reynolds number associated with the intermediate and chaotic flow regimes. Nevertheless, the LBM solver was shown to successfully capture all anticipated four flow regimes.

4 Conclusions & Future work

This study aims to investigate the capability of an in-house LBM solver to accurately capture the distinct flow phenomena in a two-dimensional double-cavity geometry subjected to incompressible and laminar flow conditions. By formulating a suitable LBM algorithm, simulations were conducted for the specified geometry and flow conditions, allowing for a comparative analysis of the results against previously published data.

The algorithm was validated with two canonical cases to evaluate whether LBM can replicate similar flow phenomena anticipated in the double-cavity case and to confirm the correctness of the algorithm implementation. The initial validation case comprised a two-dimensional circular cylinder exposed to a uniform cross-flow at a Reynolds number of $Re_D = 100$. We investigated the resultant flow field, the pressure distribution along the cylinder surface, the time-dependent lift and drag coefficients, and the Strouhal number associated with the vortex shedding. The computed results were found to be in excellent agreement with previous studies that utilized alternate methodologies under analogous flow conditions. A discrepancy was noted in the pressure distribution along the surface of the cylinder, wherein "peaks" in the pressure coefficient manifested at various locations on the surface. These peaks originated from a misalignment between the boundary condition implemented in the algorithm and the configuration defined with the computational grid. While the computational grid was Cartesian, and the boundary condition applied was appropriate for bodies with straight edges, the circular cylinder body solved here has a curved surface. This origin for the misalignment in the observed peaks was further confirmed in the subsequent validation case.

In the second validation case, we examined a two-dimensional square cylinder subjected to a fully developed channel flow. In this analysis, we investigated the same parameters as those considered in the circular cylinder case yet extended our study to encompass various Reynolds numbers. The results aligned closely with findings from previous studies and also validated the origin of the minor discrepancies noted in the circular cylinder case. Specifically, in the context of the square cylinder, the algorithm effectively simulated fully developed channel flow by employing suitable boundary conditions, and the straight edges of the body facilitated accurate enforcement of the bounce-back (BB) boundary condition.

It is noteworthy that the two validation cases can be further verified. For instance, the cylinder can be analyzed for a range of Reynolds numbers to assess the consistency of the Strouhal number. In addition, the pressure distribution along the square surface can be computed and compared for various Reynolds numbers. While there is an opportunity to continue validating these cases in greater depth, based on the promising results obtained from the two validation cases above, a decision has been made to proceed with simulating the double-cavity geometry.

The double-cavity configuration was simulated at various Reynolds numbers to characterize the different flow regimes that are expected to develop in this geometry. The resulting flow fields reveal distinct flow structures, which enable the classification of the flow into one of the following regimes: steady, periodic, intermediate, or chaotic. In the periodic regime, distinct flow structures and flow phenomena were found, as indicated by the horizontal velocity signal recorded at several points within the cavity region. The signals obtained from these measurements provided a deeper insight into the characteristics of this type of flow, such as primary vortices and shear layer oscillations.

A similar analysis was conducted for each flow regime using a single probe, offering an additional perspective on the differences between the regimes. Although the LBM algorithm successfully captured all the expected flow regimes, a discrepancy was observed with the results published by Tuerke (2017) for the Reynolds number associated with the intermediate and chaotic flow regimes. This discrepancy may stem from differences in the upstream domain size or algorithmic implementations that influence the flow field, such as applying a buffer zone to reduce acoustic wave reflections from the domain boundaries.

Beyond the analysis conducted for the double-cavity case and the two validation cases, there is room for future work to assess the reliability of the LBM computational method, its accuracy, and its suitability for problems of this type. Therefore, the following topics for future work arise:

- The validation cases, including the circular cylinder in uniform flow and the square cylinder in channel flow, can be further validated to identify potential issues in the algorithm. Among the possible validation approaches, one could examine the Strouhal number obtained for the circular cylinder across a range of Reynolds numbers and compare it with existing knowledge. Additionally, the average drag coefficient and fluctuations in the lift and drag coefficients can be analyzed for different Reynolds numbers in both the circular and square cylinder cases.
- The hypothesis that the localized errors in the pressure coefficient distribution along the circular cylinder boundary arise from adapting boundary conditions to curved surfaces can be more robustly tested by implementing alternative boundary conditions, such as immersed boundary conditions, instead of the bounce-back approach. This would allow for a further validation and accuracy assessment of the boundary conditions in non-straight boundary cases.
- Conduct an in-depth convergence analysis for both validation cases and the double-cavity geometry to determine whether the resolutions used in each simulation are sufficient to produce accurate results while avoiding excessively high resolutions that would lead to impractical runtime costs.
- Investigate the hypothesis that the implementing buffer zone is responsible for the mismatch between the observed flow regime and the characteristic Reynolds number of each regime for the double-cavity case. This can be done by testing buffer zones with varying amplification factors and distributions to verify their impact on the resulting flow regime at a given Reynolds number. A range of amplifications can be examined while noting that weaker buffer zones lead to stronger boundary condition reflections, which may reduce accuracy even if the resulting flow regime aligns more closely with the expected Reynolds number.
- Examine the impact of different double cavity geometries on the flow, including variations in channel height, cavity width-to-depth ratio, and even slightly altered cases such as asymmetrically positioned cavities relative to the horizontal axis or a single cavity of varying sizes. This approach will allow us to explore phenomena that do not occur in the currently studied geometry and assess how well the algorithm handles them.
- For a more in-depth study, additional models could be incorporated, such as a turbulence model or a compressibility model. This would provide further insights into LBM's ability to capture even more complex flow phenomena in this geometry, which do not appear in the incompressible laminar flow examined in this study.

References

Basley, J., Pastur, L., Lusseyran, F., Faure, T. M., and Delprat, N. (2011). Experimental investigation of global structures in an incompressible cavity flow using time-resolved piv. Experiments in Fluids, 50:905–918.

Breuer, M., Bernsdorf, J., Zeiser, T., and Durst, F. (2000). Accurate computations of the laminar flow past a square cylinder based on two different methods: lattice-boltzmann and finite-volume. International journal of heat and fluid flow, 21(2):186–196.

Burroughs, C. B. and Stinebring, D. R. (1994). Cavity flow tones in water. The Journal of the Acoustical Society of America, 95(3):1256–1263.

Drikakis, D. (1997). Bifurcation phenomena in incompressible sudden expansion flows. Physics of Fluids, 9(1):76–87.

Du, G., Tian, Y., Le, J., Zhong, F., and Zhang, Y. (2023). Experimental investigation of effects of dual-cavity configuration on ignition and flame stabilization in a kerosene-fueled supersonic combustor. Physics of Fluids, 35(1).

Gadoin, E., Le Quéré, P., and Daube, O. (2001). A general methodology for investigating flow instabilities in complex geometries: application to natural convection in enclosures. International Journal for Numerical methods in fluids, 37(2):175–208.

Heubes, D., Bartel, A., and Ehrhardt, M. (2014). Exact artificial boundary conditions for a lattice boltzmann method. Computers & Mathematics with Applications, 67(11):2041–2054.

Krüger, T., Kusumaatmaja, H., Kuzmin, A., Shardt, O., Silva, G., and Viggen, E. M. (2017). The lattice Boltzmann method, volume 10. Springer.

Lienhard, J. H. et al. (1966). Synopsis of lift, drag, and vortex frequency data for rigid circular cylinders, volume 300. Technical Extension Service, Washington State University Pullman, WA.

Lusseyran, F., Pastur, L., and Letellier, C. (2008). Dynamical analysis of an intermittency in an open cavity flow. Physics of Fluids, 20(11).

Maurel, A., Ern, P., Zielinska, B., and Wesfreid, J. (1996). Experimental study of self-sustained oscillations in a confined jet. Physical Review E, 54(4):3643.

Norberg, C. (2001). Flow around a circular cylinder: aspects of fluctuating lift. Journal of fluids and structures, 15(3-4):459–469.

Podvin, B., Fraigneau, Y., Lusseyran, F., and Gougat, P. (2006). A reconstruction method for the flow past an open cavity.

Righolt, B., Kenjereš, S., Kalter, R., Tummers, M., and Kleijn, C. (2015). Dynamics of an oscillating turbulent jet in a confined cavity. Physics of Fluids, 27(9).

Rizi, M.-Y., Pastur, L., Abbas-Turki, M., Fraigneau, Y., and Abou-Kandil, H. (2015). Closed-loop analysis and control of cavity shear layer oscillations. Intl J. Flow Control, 6:171–187.

Tuerke, F. (2017). Flow in a channel with two facing cavities. PhD thesis, Université Paris Saclay (COmUE); Universidad de Buenos Aires. Facultad de ....

Tuerke, F., Pastur, L., Fraigneau, Y., Sciamarella, D., Lusseyran, F., and Artana, G. (2017). Nonlinear dynamics and hydrodynamic feedback in two-dimensional double cavity flow. Journal of Fluid Mechanics, 813:1–22.

Viggen, E. (2014). The lattice boltzmann method: Fundamentals and acoustics (ph. d thesis). Norwegian University of Science and Technology, Trondheim, Norway.

Wang, L., Zhou, J., and Dong, L. (2020). Optical properties of a double-cavity system coupled to a waveguide in photonic crystals. Applied Optics, 59(15):4572–4576.

Zdravkovich, M. (1990). Conceptual overview of laminar and turbulent flows past smooth and rough circular cylinders. Journal of wind engineering and industrial aerodynamics, 33(1-2):53–62.

Zdravkovich, M. M. (1997). Flow around circular cylinders: Volume 2: Applications, volume 2. Oxford university press.

Zhou, L., Cheng, M., and Hung, K. (2005). Suppression of fluid force on a square cylinder by flow control. Journal of fluids and structures, 21(2):151–167.

Zou, Q. and He, X. (1996). On pressure and velocity flow boundary conditions and bounce back for the lattice boltzmann bgk model. eprint. arXiv preprint comp-gas/9611001.